IEEE Access
Multidisciplinary | Rapid Review | Open Access Journal

Received 23 December 2025, accepted 6 February 2026, date of publication 16 February 2026, date of current version 19 February 2026.

Digital Object Identifier 10.1109/ACCESS.2026.3665049

RESEARCH ARTICLE

Mitigating Frequency Dependent Carrier Frequency Offset in Multi-Carrier Phase Difference Ranging Through Timing Diagram Design

ALEŠ SIMONČIČ, (Student Member, IEEE), GREGA MORANO, (Graduate Student Member, IEEE), ANDREJ HROVAT, (Member, IEEE), AND TOMAŽ JAVORNIK, (Member, IEEE)

Department of Communication Systems, Jožef Stefan Institute, 1000 Ljubljana, Slovenia
Jožef Stefan International Postgraduate School, 1000 Ljubljana, Slovenia

Corresponding author: Aleš Simončič (ales.simoncic@ijs.si)

This work was supported by Slovenian Research and Innovation Agency (ARIS) under Grant J2-4461, Grant P2-0016, and Grant PR-12348.

ABSTRACT Multi-carrier phase difference (MCPD) ranging is promising for low-cost proximity and localization systems, but its performance degrades when devices use inexpensive crystal oscillators. In practice, carrier frequency offset (CFO) can change linearly with carrier frequency, and the difference between the slopes of CFO as a function of carrier frequency, referred to as the carrier frequency offset slope difference (CFOSD), introduces a systematic distance bias. We model MCPD using the standard timing diagram (TD) and derive a closed-form expression for the distance error that reveals a dominant term proportional to both CFOSD and the sampling time offset difference between devices. Two TD design approaches are proposed and validated by simulations with CFOSD sweep and additive noise. The temporal differential correction approach suppresses the effect of CFOSD on distance estimation over a wide CFOSD range and achieves almost zero bias, but at the cost of longer measurement duration, greater sensitivity to timing asynchronization, and a higher required signal-to-noise ratio (SNR). The role switching approach reverses the roles of initiator and reflector across carrier frequencies according to a role pattern, preserves the measurement duration of the standard TD, and reduces CFOSD sensitivity within a method-dependent CFOSD operating range. Experimental results for the standard and role-switching TD designs confirm the signal model, show good agreement between measured and simulated channel impulse responses, and demonstrate that the proposed TD designs substantially reduce distance bias caused by CFOSD while remaining compatible with low-cost implementations.

INDEX TERMS Asynchronization, carrier frequency offset (CFO), channel frequency response (CFR), channel impulse response (CIR), clock drift, crystal oscillator, Internet of Things (IoT), multi-carrier phase difference (MCPD), phase-based ranging (PBR), timing diagram.

I. INTRODUCTION

Integrated sensing and communication (ISAC) aims to unify communication and sensing functionalities within a common hardware platform, allowing each function to benefit from information provided by the other. In bistatic configurations, communication nodes can exploit sensing information extracted from the spatial, spectral, and temporal diversity present in the exchanged signals [1]. Short-range proximity and location information play a central role

The associate editor coordinating the review of this manuscript and approving it for publication was Li Zhang.

in many everyday applications, including public transport ticketing, parking, electronic tolling, payment and identification systems, personnel tracking, and physical access control [2]. These applications motivate the development of accurate, low-cost ranging techniques that can be integrated directly into commodity wireless devices. A major challenge in such systems is the lack of synchronization between devices, which can introduce ranging ambiguities and prevent coherent processing of discontinuous measurements [3].

Phase-based ranging (PBR) has gained popularity because it enables decimeter-level accuracy in indoor scenarios [4]. Multi-carrier phase difference (MCPD) extends PBR by acquiring phase measurements across several carrier frequencies using two ranging devices: the initiator (INIT) and the reflector (REF) [5]. This technique provides a larger unambiguous range, reduced multipath sensitivity, and cancellation of random phase-locked loop (PLL)-induced phase offsets across discontinuous transmissions on different frequencies. With low hardware complexity and low energy consumption, MCPD is particularly attractive for low-cost wireless systems.

The imperfections of low-cost crystal oscillators used for both radio frequency (RF) synthesis and timing affect MCPD performance by introducing carrier frequency offset (CFO) and clock drift, which can bias distance estimation. Crystal oscillators are characterized by frequency tolerance and frequency stability, which depend on environmental conditions such as temperature, supply voltage, load capacitance, humidity, pressure, aging, etc. As these conditions vary, the instantaneous frequencies of the crystal oscillators in the two devices involved in ranging can drift differently over time. Although initial calibration between devices can compensate for static biases, environmental changes make such calibration invalid and degrade ranging accuracy. Using higher-grade clock sources would reduce environment-dependent effects on distance estimation but would increase costs. A single highly accurate reference clock, such as one provided by the global navigation satellite system (GNSS), can be distributed wirelessly or via a wired link, but this approach adds complexity, is meaningful only for static anchors in the case of wired clock distribution, and is impractical when only a small number of devices need to be synchronized [3]. These limitations motivate the development of MCPD ranging procedures that are inherently less sensitive to variations in crystal oscillator performance. In particular, we study how to mitigate distance estimation errors in MCPD ranging caused by CFO with a linear dependence on the carrier frequency, which occurs in PLL-based carrier frequency synthesis, where the reference frequency error is multiplied by a carrier-dependent factor, scaling the error proportionally across the carriers. The difference between the slopes of CFO as a function of carrier frequency for the two devices, referred to as the carrier frequency offset slope difference (CFOSD), then produces a systematic distance bias.

Clock and frequency synchronization has been studied extensively in wireless communications [6], [7], ultra-wideband (UWB) ranging [8], and ISAC systems [3]. However, dynamic synchronization aspects in MCPD have received little attention. Previous works address interference mitigation [9], algorithmic improvements [4], [10], [11], or comparisons of localization techniques [12], [13], but do not explicitly model time and frequency misalignment between devices. Asynchronization between devices is typically ignored, mitigated by initial calibration at known distances, or suppressed by assuming high-quality crystal oscillators [14].

The impact of asynchronization on MCPD ranging has been addressed in the following literature. The authors in [15] jointly analyzed timing asynchronization and CFO, proposing to measure the CFO, map it to the underlying crystal offset difference, and correct the phase measurements accordingly. Group-ranging scenarios were examined in [16] and [17], showing that asynchronization has an even stronger impact in multi-device setups. In [17], a technique was proposed in which the INIT shifts the timeslots of REFs in consecutive measurements to estimate crystal offsets. Estimating CFO from multiple phase samples acquired at a single carrier frequency and then correcting the measured phase samples to remove CFO-induced phase shifts was proposed in [18]. While CFO can be estimated during the measurement and compensated for, accurate estimation requires a large number of additional samples [19]. This remains feasible under the assumption that the CFO is constant across the measurement band, since the estimation can be performed at only one frequency. However, when the CFO varies with carrier frequency, this approach becomes impractical, as CFO would have to be estimated separately at each carrier, substantially increasing the measurement duration. Even under the assumption that CFO varies linearly, estimation would need to be performed at least at two carrier frequencies, followed by interpolation or extrapolation.

An approach involving four transmissions per carrier frequency, in which an INIT→REF exchange is followed by a REF→INIT exchange to suppress the impact of a constant CFO in MCPD ranging, was proposed in [20]. We build on this idea and consider timing diagram (TD) optimization with the objective of structurally reducing the effect of CFOSD without requiring explicit CFO estimation at each carrier frequency. While TD optimization for MCPD has received limited attention beyond [20], it has been extensively explored in related time-based ranging systems, particularly in the UWB domain. UWB ranging typically resolves timing offset using the single-sided two-way ranging (SS-TWR) procedure and further suppresses clock drift through the double-sided two-way ranging (DS-TWR) technique [21]. Numerous works have proposed TD refinements to reduce clock-drift-induced bias, often balancing the trade-off between the number of transmissions and estimation accuracy [8], [22], [23], [24], [25], [26]. Additional transmissions have also

been used to obtain extra phase samples that compensate for phase drift due to CFO in UWB system that combine PBR principles, as shown in [22]. In [27], TD parameters have been optimized using Cramer-Rao lower bound (CRLB) analysis, which shows that longer second-response delays reduce estimator variance but simultaneously lower the number of measurements per unit time, thus increasing the overall variance of combined estimates. Sequential time difference of arrival (TDoA) approaches [28] can also avoid explicit timing synchronization between the tag and anchors, but they require at least three anchors with known geometry and remain more sensitive to clock drift than two-way ranging (TWR) procedures.

Among the contributions of this work is a dynamic role-switching scheme within the MCPD procedure to decouple the phase shifts introduced by CFOSD from those caused by signal propagation, thereby reducing the resulting bias in the estimated distance. A conceptually related switching approach was presented in our earlier work [19], where the order of carrier frequencies used in the MCPD procedure was optimized to decouple phase shifts caused by clock-drift differences from those due to propagation, assuming a frequency-independent CFO across the carrier set. This work extends that research by addressing CFOSD, which introduces an additional bias term that frequency order optimization alone cannot remove. Similar switching-related strategies have been explored in adjacent domains such as frequency-modulated continuous wave (FMCW) radar [29], [30], [31], [32], channel sounding [33], [34], [35], [36], [37], and direction-of-arrival (DoA) estimation [38], [39].

The objective of this work is to mitigate the effect of CFOSD on MCPD distance estimation without requiring explicit CFO estimation. We achieve this by modifying the MCPD TD to either structurally cancel CFOSD-induced phase shifts or decouple them from the propagation-induced phase shifts, thereby reducing the resulting bias without extending the measurement duration. The contributions of this paper are:

- Identification and modeling of CFOSD as a previously unaddressed source of systematic bias in MCPD, supported by analytical derivations and measurements.
- Design of TDs that suppress the effect of CFOSD on distance estimation by using temporal-differential correction and dynamic role-switching approaches.
- Evaluation of the effectiveness of the proposed TDs in simulations under noise-free and noisy conditions.
- Experimental validation of TDs based on the dynamic role-switching approach.

The remainder of the paper is organized as follows. Section II presents the signal model and analyzes the CFOSD impact on MCPD distance estimation. The proposed TD optimization approaches are described in Section III. Simulation and experimental evaluations follow in Sections IV and V, respectively. The paper concludes with Section VI.

TABLE 1. List of key acronyms and symbols.

Acronym / Symbol	Description
M	Number of carrier frequencies
i	Carrier frequency index, $i \in \{0, \ldots, M-1\}$
$P[i]$	Vector defining the order in which the carrier frequencies are applied during the MCPD procedure
ν	Carrier spacing
$f_c^{(i)}$	Nominal carrier frequency of the i-th carrier
$f_I^{(i)}, f_R^{(i)}$	Actual carrier frequencies of the i-th carrier generated by INIT and REF
$\Delta f_I^{(i)}, \Delta f_R^{(i)}$	CFOs of INIT and REF of the i-th carrier
$\Delta f^{(i)}$	Effective CFO between devices of the i-th carrier, $\Delta f^{(i)} = \Delta f_I^{(i)} - \Delta f_R^{(i)}$
$\Delta f_{0,I}, \Delta f_{0,R}$	Initial CFO values at $f_c^{(0)}$ for INIT and REF
Δf_0	Difference between initial CFO values, $\Delta f_0 = \Delta f_{0,I} - \Delta f_{0,R}$
$k_{\mathrm{CFO},I}, k_{\mathrm{CFO},R}$	Linear slopes of CFO as a function of carrier frequency for INIT and REF
CFOSD	Carrier frequency offset slope difference, $k_{\mathrm{CFO},I} - k_{\mathrm{CFO},R}$
f_{IF}	Intermediate frequency
ΔT_s	Nominal time difference between the start of two consecutive carrier measurements
$T_{o,R}, T_{o,I}$	Nominal time sampling offsets at REF and INIT after the start of the measurement on each carrier
ΔT_o	Time sampling offset difference, $\Delta T_o = T_{o,R} - T_{o,I}$
e_I, e_R	Relative frequency errors of the timing oscillators at INIT and REF
$\Theta_{\mathrm{LO},I}^{(i)}, \Theta_{\mathrm{LO},R}^{(i)}$	Local oscillator initial phase offsets of the i-th carrier at INIT and REF
$RP[i]$	Role pattern, $RP[i] = 1$ for standard roles and $RP[i] = -1$ for reversed roles

To improve readability, Table 1 summarizes the key acronyms and symbols used in this paper.

II. SIGNAL MODEL AND PROBLEM FORMULATION

Most existing research on MCPD assumes that the CFO of each device is constant across the measurement band. In practice, CFO can be frequency dependent as PLL-based carrier frequency generation is achieved by multiplying the crystal oscillator reference frequency f_{ref} by the carrier-dependent factor $k^{(i)}$ to synthesize the desired carrier frequency $f_c^{(i)} = f_{ref} \cdot k^{(i)}$, where $i \in \{0, \ldots, M-1\}$ is the carrier index and M is the number of carriers used in MCPD. A deviation in the reference oscillator frequency from its nominal value by a multiplicative error e causes the actual reference to be $f'_{ref} = f_{ref}(1+e)$. With uniform carrier spacing ν, the carrier frequency at index i can be expressed in terms of the nominal carrier frequency $f_c^{(0)}$ at $i = 0$ as

$$f_c^{(i)} = f_c^{(0)} + e f_c^{(0)} + (1+e)\, i\, \nu, \tag{1}$$

which shows that the frequency error increases linearly with the carrier index and that the slope of this increase is proportional to the oscillator error e. To examine this effect in practice, we measured the CFO across carrier frequencies for four devices equipped with AT86RF215 radio modules [40].

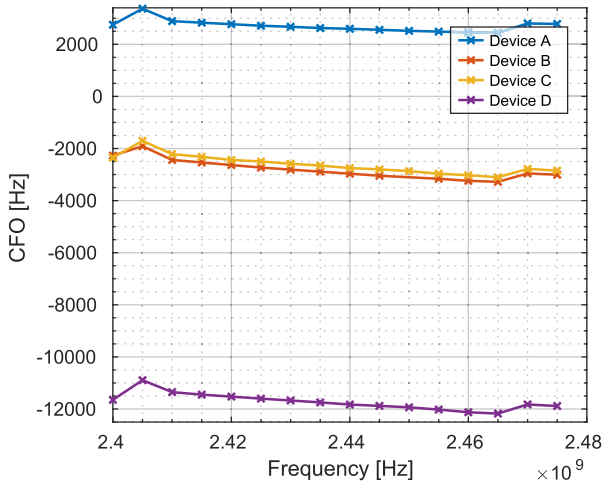

FIGURE 1. Measured CFOs as a function of carrier frequency for four devices equipped with AT86RF215 radio modules, showing a clear linear CFO trend with distinct initial CFO offsets.

TABLE 2. CFO slope values obtained from the measurements in Fig. 1, expressed as the change in CFO per MHz to make the numerical values more interpretable.

	Device A	Device B	Device C	Device D
$k_{CFO}\ \left[\frac{\text{Hz}}{\text{MHz}}\right]$	-5.46	-13.49	-12.90	-10.79

As shown in Fig. 1, all devices exhibit a clear linear CFO trend with frequency. Table 2 lists the corresponding slopes computed using simple linear regression. The differences between slopes confirm the presence of CFOSD and motivate deriving the signal model to quantify its impact on distance estimation.

We derive a signal model for the standard TD configuration used in MCPD ranging, as shown in Fig. 2(a), which also serves as the basis for the TD optimization in the next section. In the standard TD configuration, REF samples the received signal at a time offset $T_{o,R}$ and INIT at a time offset $T_{o,I}$ after the start of the measurement on each carrier. The time difference between the start of two consecutive carrier measurements is denoted by ΔT_s. The actual sampling instants deviate from the ideally defined times due to the clock drift of each device. Non-ideal sampling times are denoted by a prime superscript and are obtained by scaling the ideal times by the reciprocal of the oscillator frequency error, that is, $(1+e_I)^{-1}$ for INIT and $(1+e_R)^{-1}$ for REF, where e_I and e_R are the dimensionless relative frequency errors of the INIT and REF crystal oscillators, typically specified in parts per million (ppm). The signal model uses separate crystal oscillators for timing and RF carrier generation at INIT and REF, which allows the contributions of clock drift and CFO to the measured phases to be observed independently. The frequency deviations of the crystal oscillators are assumed constant during a single MCPD measurement sequence, and propagation is modeled as free space with REF transmitting and receiving at carrier frequencies that are offset by the intermediate frequency f_{IF}, analogous to the formulation in [19].

The nominal carrier frequency of the i-th carrier is

$$f_c^{(i)} = f_c^{(0)} + i\,\nu.$$

The actual carrier frequencies generated by INIT and REF, affected by crystal-oscillator inaccuracies, are denoted by $f_I^{(i)}$ and $f_R^{(i)}$, respectively. Their corresponding CFO values relative to the nominal carrier,

$$\Delta f_I^{(i)} = f_I^{(i)} - f_c^{(i)}, \qquad \Delta f_R^{(i)} = f_R^{(i)} - f_c^{(i)},$$

represent the individual CFOs of the devices. The effective CFO between INIT and REF on the i-th carrier is defined as

$$\Delta f^{(i)} = \Delta f_I^{(i)} - \Delta f_R^{(i)}.$$

The signal model describing the phase samples acquired at INIT and REF for MCPD with the standard TD configuration, including arbitrary ordering of carrier frequency, was derived in [19]. Considering that one phase sample is acquired per carrier frequency ($n = 0$), the sampled phase at REF for the i-th carrier is

$$\begin{aligned}\phi_{R,0}^{(i)} = {} & 2\pi\left(f_{IF} + \Delta f^{(i)}\right)\left(P[i]\cdot\Delta T'_{s,R} + T'_{o,R}\right) \\ & - 2\pi\left(f_c^{(i)} + \Delta f_I^{(i)}\right)\frac{d}{c} \\ & + \Theta_{LO,I}^{(i)} - \Theta_{LO,R}^{(i)},\end{aligned} \tag{2}$$

where c is the speed of light, d is the distance between the devices, $\Delta T'_{s,R}$ is the non-ideal measurement of the interval ΔT_s at REF due to its own clock drift, $\Theta_{LO,I}^{(i)}$ and $\Theta_{LO,R}^{(i)}$ denote the local oscillator initial phase offsets of the i-th carrier at INIT and REF, and $P[i]$ is the vector that defines the order in which the carrier frequencies are applied during the MCPD procedure [19]. The indices of $P[i]$ correspond to the ordered carrier frequencies from the lowest ($i = 0$) to the highest ($i = M-1$) used in MCPD, and each value P_i specifies when in the sequence the particular carrier frequency with index i is used in the MCPD procedure, with the first position corresponding to value 0. We assume that each carrier frequency is used exactly once in the sequence.

The corresponding phase sampled at INIT for the i-th carrier is

$$\begin{aligned}\phi_{I,0}^{(i)} = {} & 2\pi\left(f_{IF} + \Delta f^{(i)}\right)\left(P[i]\cdot\Delta T'_{s,I} + T'_{o,I}\right) \\ & + 2\pi\left(f_c^{(i)} - f_{IF} + \Delta f_R^{(i)}\right)\frac{d}{c} \\ & + \Theta_{LO,I}^{(i)} - \Theta_{LO,R}^{(i)},\end{aligned} \tag{3}$$

where $\Delta T'_{s,I}$ is the non-ideal measurement of interval ΔT_s at INIT due to its own clock drift.

To cancel the unknown initial phase offsets of the local oscillators, the final phase for the i-th carrier is obtained by subtracting the phase samples acquired at INIT (3) from

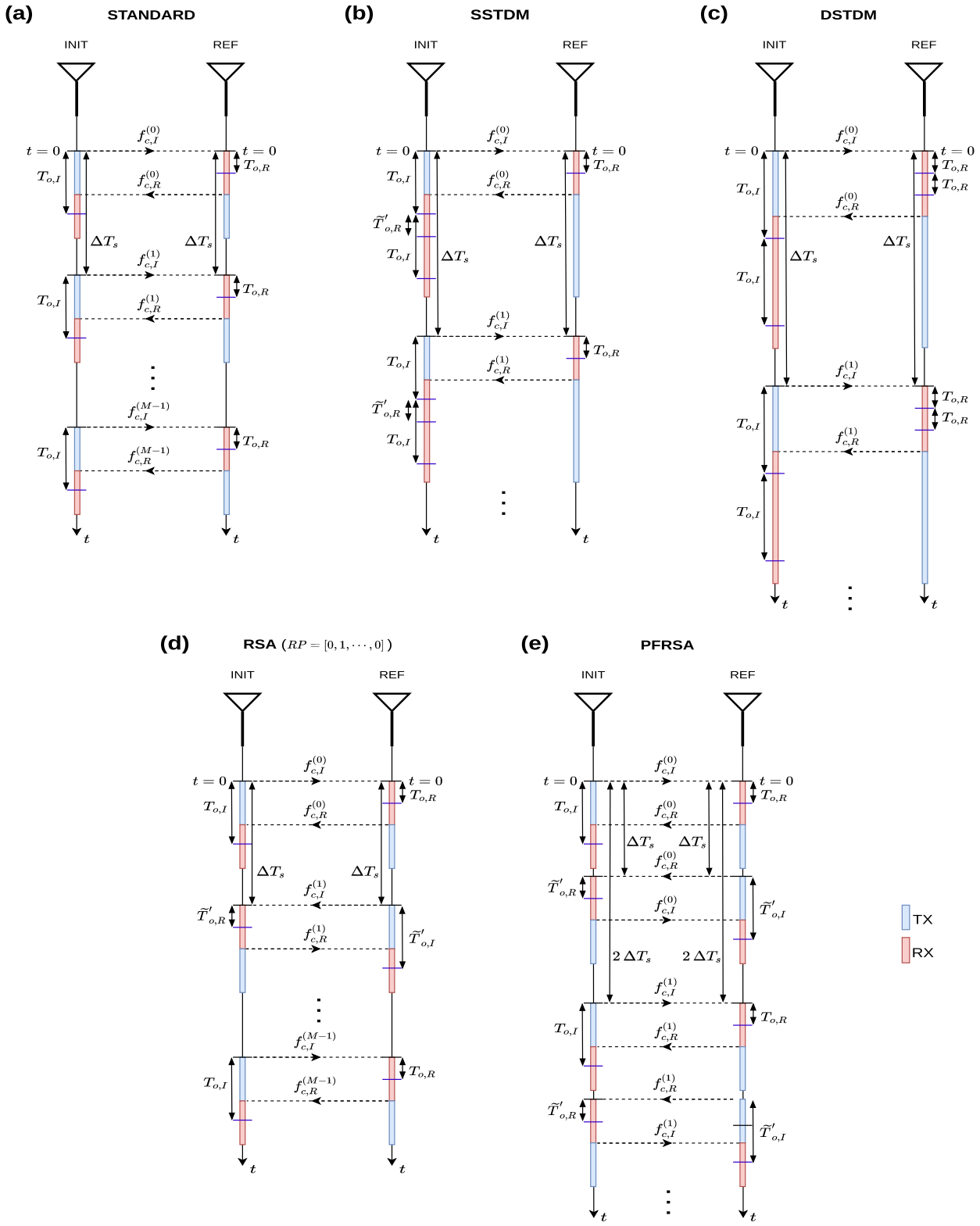

FIGURE 2. TDs for MCPD ranging. (a) Standard TD: INIT and REF sample at fixed offsets on every carrier. (b) SSTDM: INIT acquires additional samples relative to its standard sampling time to suppress the CFOSD-induced phase component. (c) DSTDM: both INIT and REF acquire additional samples, enabling full cancellation of the CFOSD contribution. (d) RSA: a role-switching approach in which INIT and REF alternate roles according to a predefined *RP* vector. (e) PFRSA: on each carrier the measurement is first performed according to the standard TD approach and then repeated with the reversed roles.

REF (2)

$$\phi^{(i)} = \phi^{(i)}_{R,0} - \phi^{(i)}_{I,0} = 2\pi\left(f_{IF} + \Delta f^{(i)}\right)\cdot \left[P[i]\,\Delta T_s \frac{e_I - e_R}{1 + e_I + e_R + e_I\,e_R} + \left(T_{o,R}\left(1+e_R\right)^{-1} - T_{o,I}\left(1+e_I\right)^{-1}\right)\right] - 2\pi\left(2f_c^{(i)} + \Delta f_I^{(i)} + \Delta f_R^{(i)} - f_{IF}\right)\frac{d}{c}. \quad (4)$$

The phase $\phi^{(i)}$ contains two bracketed phase terms scaled by $\Delta f^{(i)}$ that are therefore affected by CFOSD. The first phase term captures timing asynchronization caused by clock drift over the measurement procedure and is proportional to the vector $P[i]$ and the relative frequency mismatch between the timing oscillators of INIT and REF, $(e_I - e_R)$. Assuming the CFO is constant across the measured band, this timing asynchronization effect on distance estimation can be efficiently mitigated using the technique in [19], where the frequency switching pattern (FSP), and therefore $P[i]$, is optimized to suppress bias from clock drift differences. Even with frequency-dependent CFO and nonzero CFOSD, the first term contributes negligibly to the CFOSD-induced distance bias. The CFOSD-induced bias is instead dominated by the second phase term in brackets, which depends approximately on the sampling time offset difference between INIT and REF.

To isolate the effect of CFOSD on MCPD distance estimation, we first neglect timing asynchronization by setting $e_I = e_R = 0$. Furthermore, the CFO is modeled as a linear function of the carrier index, and for the i-th carrier it is expressed as

$$\Delta f_I^{(i)} = \Delta f_{0,I} + k_{\mathrm{CFO},I}\; i\; \nu,$$
$$\Delta f_R^{(i)} = \Delta f_{0,R} + k_{\mathrm{CFO},R}\; i\; \nu, \quad (5)$$

where $\Delta f_{0,I}$ and $\Delta f_{0,R}$ denote the initial CFO values at INIT and REF at the beginning of the measured frequency band, and $k_{\mathrm{CFO},I}$ and $k_{\mathrm{CFO},R}$ are their respective CFO slopes with respect to carrier frequency. The CFOSD is equal to $k_{\mathrm{CFO},I} - k_{\mathrm{CFO},R}$.

Expanding the terms $\Delta f^{(i)}$, $f_c^{(i)}$, $\Delta f_I^{(i)}$, and $\Delta f_R^{(i)}$ and substituting the CFO model from (5) into (4), the phase difference for the i-th carrier becomes

$$\phi^{(i)} = 2\pi\left(f_{IF} + \Delta f_0\right)\cdot \Delta T_o + 2\pi\left(k_{\mathrm{CFO},I} - k_{\mathrm{CFO},R}\right)\cdot i\cdot \nu\cdot \Delta T_o - 2\pi\left(2f_c^{(0)} - f_{IF} + \Delta f_{0,I} + \Delta f_{0,R}\right)\frac{d}{c} - 2\pi\cdot i\cdot\left(2 + k_{\mathrm{CFO},I} + k_{\mathrm{CFO},R}\right)\cdot \nu\,\frac{d}{c}, \quad (6)$$

where $\Delta T_o = T_{o,R} - T_{o,I}$ is the sampling time offset difference between devices, and $\Delta f_0 = \Delta f_{0,I} - \Delta f_{0,R}$ denotes the difference between the initial CFO values at the beginning of the measured frequency band of INIT and REF.

The last term in (6) includes the expected linear phase change with carrier index i due to signal propagation. However, the second term, which depends on CFOSD, also exhibits a linear dependence on i. As a result, the CFOSD-induced phase shifts as a function of carrier index i are coupled with the propagation-induced phase shifts, producing a systematic bias in the distance estimate. In MCPD, the distance estimate is obtained from the slope of the measured phase with respect to carrier frequency [2], i.e.,

$$\hat{d} = -\frac{c}{4\pi}\frac{\phi^{(i+1)} - \phi^{(i)}}{\nu}. \quad (7)$$

By inserting (6) into (7) and comparing the resulting slope with the ideal CFOSD-free case, the distance bias E introduced by CFOSD is

$$E = \frac{c}{2}\cdot\left(k_{\mathrm{CFO},I} - k_{\mathrm{CFO},R}\right)\cdot \Delta T_o - \frac{1}{2}\left(k_{\mathrm{CFO},I} + k_{\mathrm{CFO},R}\right)\cdot d. \quad (8)$$

The bias expression has two components. The first term depends linearly on the CFOSD and the sampling time offset difference between INIT and REF, ΔT_o. The second term depends on the sum of the CFO slopes and the true distance d. We quantify their relative contributions using example parameters: $k_{\mathrm{CFO},I} = 10\ \frac{\mathrm{Hz}}{\mathrm{MHz}}$, $k_{\mathrm{CFO},R} = 0$, $d = 10$ m, and $\Delta T_o = 120\ \mu$s, which is the approximate sampling time offset difference in our experimental setup. The first term contributes approximately 18 cm of bias, while the second term contributes only about 50 μm, indicating that the second term is negligible, even though it scales with distance. Minimizing CFOSD-induced bias requires the sampling time offset difference ΔT_o to be as small as possible, but in practice, ΔT_o is constrained by hardware capabilities and cannot be made arbitrarily small.

Although the distance estimate can be obtained directly from (7), in practice, a larger set of carrier frequencies is used, and the complex samples acquired at those carriers together form the channel frequency response (CFR). The channel impulse response (CIR) is then obtained by applying the inverse fast Fourier transform (IFFT) to the CFR, and the distance is estimated from the position of the dominant peak in the CIR.

III. TIMING DIAGRAM OPTIMIZATION

This section describes two TD modification approaches that reduce the impact of CFOSD on distance estimation without requiring explicit CFO estimation. The first approach augments standard TD by acquiring additional samples at INIT or at both devices at specific time instants relative to the standard sampling times. These additional samples are combined with those obtained under standard TD using a temporal differential correction approach (TDCA), which suppresses the CFOSD-induced contribution to the overall sampled phase. The second approach dynamically switches the roles of INIT and REF during the MCPD procedure, effectively alternating which device transmits first and which

listens, to decouple CFOSD-induced phase shifts from those caused by propagation. For completeness, a third TD modification proposed in [20] is discussed at the end of this section.

A. TEMPORAL DIFFERENTIAL CORRECTION APPROACH

Two TD optimization methods based on TDCA are proposed. The first is called the *single-sided temporal differential method* (SSTDM) and is illustrated in Fig. 2(b). For the i-th carrier, the phase samples $\phi_{R,0}^{(i)}$ and $\phi_{I,0}^{(i)}$ are acquired at REF and INIT at the same time instants as in the standard TD, that is, at $T'_{o,R}$ and $T'_{o,I}$, respectively. Then, two additional samples are acquired at INIT: the first at $T'_{o,I} + \widetilde{T}_{o,R}$ and the second at $2 \cdot T'_{o,I}$ after the start of the measurement on each carrier. Here, $\widetilde{T}_{o,R}$ denotes the nominal REF sampling offset $T_{o,R}$ as measured on INIT and is therefore affected by INIT's clock drift rather than REF's. In contrast to Section II, where timing asynchronization from clock drift differences was neglected to isolate the CFOSD effect, it is now reintroduced to quantify how the proposed TD designs also affect the timing asynchronization contribution to the distance bias. The phase sample taken at time $T'_{o,I} + \widetilde{T}_{o,R}$ is

$$\begin{aligned}\phi_{I,1}^{(i)} &= 2\pi\left(f_{IF} + \Delta f^{(i)}\right)\left(P[i]\cdot\Delta T'_{s,I} + T'_{o,I} + \widetilde{T}_{o,R}\right)\\ &\quad + 2\pi\left(f_c^{(i)} - f_{IF} + \Delta f_R^{(i)}\right)\frac{d}{c}\\ &\quad + \Theta_{LO,I}^{(i)} - \Theta_{LO,R}^{(i)}.\end{aligned} \tag{9}$$

Similarly, the phase sample taken at time $2 \cdot T'_{o,I}$ is

$$\begin{aligned}\phi_{I,2}^{(i)} &= 2\pi\left(f_{IF} + \Delta f^{(i)}\right)\left(P[i]\cdot\Delta T'_{s,I} + 2\,T'_{o,I}\right)\\ &\quad + 2\pi\left(f_c^{(i)} - f_{IF} + \Delta f_R^{(i)}\right)\frac{d}{c}\\ &\quad + \Theta_{LO,I}^{(i)} - \Theta_{LO,R}^{(i)}.\end{aligned} \tag{10}$$

The final phase sample for the i-th carrier is obtained by combining the four samples according to

$$\begin{aligned}\phi^{(i)} &= \phi_{R,0}^{(i)} - \phi_{I,0}^{(i)} + (\phi_{I,2}^{(i)} - \phi_{I,0}^{(i)}) - (\phi_{I,1}^{(i)} - \phi_{I,0}^{(i)})\\ &= 2\pi\left(f_{IF} + \Delta f^{(i)}\right)\cdot\\ &\quad\left[P[i]\,\Delta T_s\,\frac{e_I - e_R}{1 + e_I + e_R + e_I\,e_R}\right.\\ &\quad\left. + T_{o,R}\,\frac{e_I - e_R}{1 + e_I + e_R + e_I\,e_R}\right]\\ &\quad - 2\pi\left(2f_c^{(i)} + \Delta f_I^{(i)} + \Delta f_R^{(i)} - f_{IF}\right)\frac{d}{c}.\end{aligned} \tag{11}$$

Compared to the standard TD approach, in which the second phase term in the brackets of (4) introduces the dominant CFOSD-induced distance bias and depends approximately on the sampling time offset difference between INIT and REF, SSTDM reduces this term to a component that depends only on the REF sampling offset $T_{o,R}$, scaled by the relative frequency mismatch between the crystal oscillators used for timing at INIT and REF. This phase component remains because INIT and REF measure the nominal offset $T_{o,R}$ differently due to their respective clock drifts.

The second TDCA-based method, called the *dual-sided temporal differential method* (DSTDM) and shown in Fig. 2(c), builds on SSTDM by eliminating the remaining timing-asynchronization term proportional to $T_{o,R}$. Two additional samples are acquired compared to the standard TD: $\phi_{R,1}^{(i)}$ at REF at time $2{\cdot}T'_{o,R}$ and $\phi_{I,1}^{(i)}$ at INIT at time $2{\cdot}T'_{o,I}$ after the start of the measurement on each carrier. The expressions for the additional phase samples are derived analogously to the SSTDM case. The final phase sample for the i-th carrier is

$$\begin{aligned}\phi^{(i)} &= 2\cdot\phi_{R,0}^{(i)} - \phi_{R,1}^{(i)} - (2\cdot\phi_{I,0}^{(i)} - \phi_{I,1}^{(i)})\\ &= 2\pi\left(f_{IF} + \Delta f^{(i)}\right)P[i]\,\Delta T_s\,\frac{e_I - e_R}{1 + e_I + e_R + e_I\,e_R}\\ &\quad - 2\pi\left(2f_c^{(i)} + \Delta f_I^{(i)} + \Delta f_R^{(i)} - f_{IF}\right)\frac{d}{c}.\end{aligned} \tag{12}$$

Although SSTDM and DSTDM effectively suppress the effect of CFOSD on distance estimation, they do so at the cost of a longer measurement interval, as both operate with a larger ΔT_s than the standard TD, with DSTDM requiring the longest duration. A longer measurement procedure increases the risk of interference, raises energy consumption, reduces the refresh rate of distance measurements, and amplifies the effect of timing asynchronization on distance estimation, as the phase shift associated with the first phase term of (11) and (12) increases with ΔT_s [19]. An increased measurement time can also exceed the channel coherence time T_c, which can be approximated as $T_c \approx 1/(2f_d)$, where f_d is the Doppler frequency shift. For example, in typical indoor environments that involve human motion, Doppler shifts in the 2.4 GHz band are usually below 12 Hz, corresponding to a coherence time of approximately 40 ms [41]. Another drawback of TDCA arises when the required sampling instants are implemented in software, making it difficult to achieve true timing symmetry due to nondeterministic delays such as operating system scheduling, interrupt handling during the measurement procedure, and other software-induced timing variations.

B. ROLE-SWITCHING APPROACH (RSA)

The RSA approach improves on the previously discussed TDCA methods by preserving the same measurement duration as the standard TD approach while reducing the bias caused by CFOSD through dynamic switching of the roles of INIT and REF during the MCPD procedure. In the standard configuration, INIT first transmits the unmodulated continuous wave (CW) and REF samples the phase, after which REF transmits and INIT samples. When the roles are reversed, REF transmits first and INIT performs the initial sampling, followed by INIT transmitting and REF sampling. We define a role pattern vector RP of length M, where each entry corresponds to one of the M ordered carrier frequencies. An entry $RP[i] = -1$ indicates that the roles are reversed for the i-th carrier, while $RP[i] = 1$ indicates that the roles follow

the standard configuration. The general principle of the RSA approach is illustrated in Fig. 2(d).

The effect of reversing roles on the sampled phase is most apparent when timing asynchronization is neglected (i.e., $e_I = e_R = 0$) and only the CFO contribution is considered. Under this assumption, the phase terms in (6) that depend on ΔT_o, change sign when the roles are reversed. Applying the role pattern RP to the MCPD procedure is therefore equivalent to multiplying the ΔT_o-dependent terms by the corresponding entry in RP, which gives

$$\begin{aligned}\phi_{RP}^{(i)} = \; & 2\pi \left(f_{IF} + \Delta f_0\right) \cdot \Delta T_o \cdot RP[i] \\ & + 2\pi \left(k_{\mathrm{CFO},I} - k_{\mathrm{CFO},R}\right) \cdot i \cdot \nu \cdot \Delta T_o \cdot RP[i]. \end{aligned} \tag{13}$$

The design objective for RSA is to determine RP such that $\phi_{RP}^{(i)}$, as a function of the carrier index i, has zero phase slope across carrier frequencies and therefore does not bias the distance estimate. The slope of $\phi_{RP}^{(i)}$ with respect to i is obtained by simple linear regression and is proportional to

$$k \propto \left(\alpha + \tfrac{M-1}{2}\beta\right) \cdot \sum_{i=-\frac{M-1}{2}}^{\frac{M-1}{2}} i \cdot RP[i] \quad + \quad \alpha \cdot \sum_{i=-\frac{M-1}{2}}^{\frac{M-1}{2}} i^2 \cdot RP[i], \tag{14}$$

where the carrier index i has been redefined to be centered around zero, $\alpha = 2\pi \left(f_{IF} + \Delta f_0\right) \cdot \Delta T_o$, and $\beta = 2\pi \left(k_{\mathrm{CFO},I} - k_{\mathrm{CFO},R}\right) \cdot \nu \cdot \Delta T_o$. Setting the slope to zero yields the following two conditions for the RP:

$$\sum_{i=-\frac{M-1}{2}}^{\frac{M-1}{2}} i \cdot RP[i] = 0, \qquad \sum_{i=-\frac{M-1}{2}}^{\frac{M-1}{2}} i^2 \cdot RP[i] = 0. \tag{15}$$

RPs that satisfy both conditions are good candidates, but they do not guarantee unbiased distance estimation when the distance is obtained from the position of the dominant peak in the CIR after applying the IFFT to the CFR. Using an RP with entries that are not all equal introduces phase discontinuities across carriers at each role change, which generate artificial paths in the CIR that can interfere with the line-of-sight (LOS) peak and affect its position. An exhaustive search for an optimal RP is computationally infeasible, as there are 2^M possible patterns. This motivates the use of structured RP designs. In the following, three different methods based on different RP designs are introduced to illustrate how different realizations of RP affect the resulting phase samples and the corresponding CIR, and are analyzed further throughout the paper. All three patterns satisfy the first condition in (15) and have a second sum that is close to zero. Additionally, the artificial peaks they generate have minimal influence on the LOS peak.

All patterns are designed for $M = 76$ carriers spanning the 2405-2480 MHz band, yielding a carrier spacing of $\nu = 1$ MHz. This matches the 1 MHz channel indexing used by the Bluetooth Low Energy (BLE) Channel Sounding feature based on MCPD, reflecting a practically relevant configuration. This configuration is used throughout the paper.

The first RSA method, called *alternating roles every frequency* (AR1), reverses roles every second carrier, corresponding to $RP = [1, -1, 1, -1, \ldots]$, with one additional adjustment: the alternating sequence is interrupted at one carrier index above the midpoint of the band and restarted with the negative value of the first element. This break is necessary to ensure that the slope of (14) is close to zero.

The RP of the second method, called *alternating roles every two frequencies* (AR2), consists of repeating blocks of $[1, -1, -1, 1]$. Since a single block satisfies the first condition in (15), the entire RP also satisfies this condition. The switching rate of the role changes is half that of AR1, so phase discontinuities across the frequency band are less frequent, which shifts the positions of the artificial peaks in the computed CIR compared to AR1.

The third method, called the *progressively less-frequent role-switching method* (PLFRSM), is designed to distribute the artificial path components in the CIR over a wider delay range and reduce their peak amplitudes compared to AR1 and AR2. To achieve this, RP uses progressively longer segments of identical values before switching to a different value, resulting in less frequent role changes as the carrier index increases. The pattern starts with the block, which is also used by AR2: $[1, -1, -1, 1]$. The next block doubles the length of the previous block, so the k-th block consists of a run of k consecutive $+1$ elements, followed by $2 \cdot k$ consecutive -1 elements, and then another run of k consecutive $+1$ elements. All blocks satisfy the first condition in (15). Because the total number of carrier frequencies is fixed, the final block may not fit entirely within the available band. In that case, the sequence is truncated at the end of the last block, and the remaining elements of RP are filled using the AR1 pattern.

Examples of simulated phase samples for the proposed methods and standard TD approach, for a fixed CFOSD values of 0 and 10 $\frac{\mathrm{Hz}}{\mathrm{MHz}}$ and different values of Δf_0, are shown in Fig. 3. The distance is set to zero, and timing asynchronization is neglected ($e_I = e_R = 0$) to clearly isolate the biasing effect of CFOSD. The remaining simulation parameters are $T_{o,R} = 105\ \mu$s, $T_{o,I} = 225\ \mu$s, $\Delta T_s = 279.5\ \mu$s, and $f_{IF} = 1$ MHz, which closely match the values used in the experimental validation with the available hardware. Fig. 4 shows the corresponding computed CIR magnitudes for a fixed CFOSD of 10 $\frac{\mathrm{Hz}}{\mathrm{MHz}}$.

The blue curve in all plots in Fig. 3 shows the phase samples for the ideal case when CFOSD $= 0$ and $\Delta f_0 = 0$. Since the distance is zero, the phase shifts due to propagation are equal for all carriers, resulting in a zero phase slope. In the standard TD approach, a nonzero CFOSD produces a linear phase trend across carriers, which is proportional to the bias in the estimated distance. The greater the absolute value of CFOSD, the larger the phase slope and the resulting distance bias.

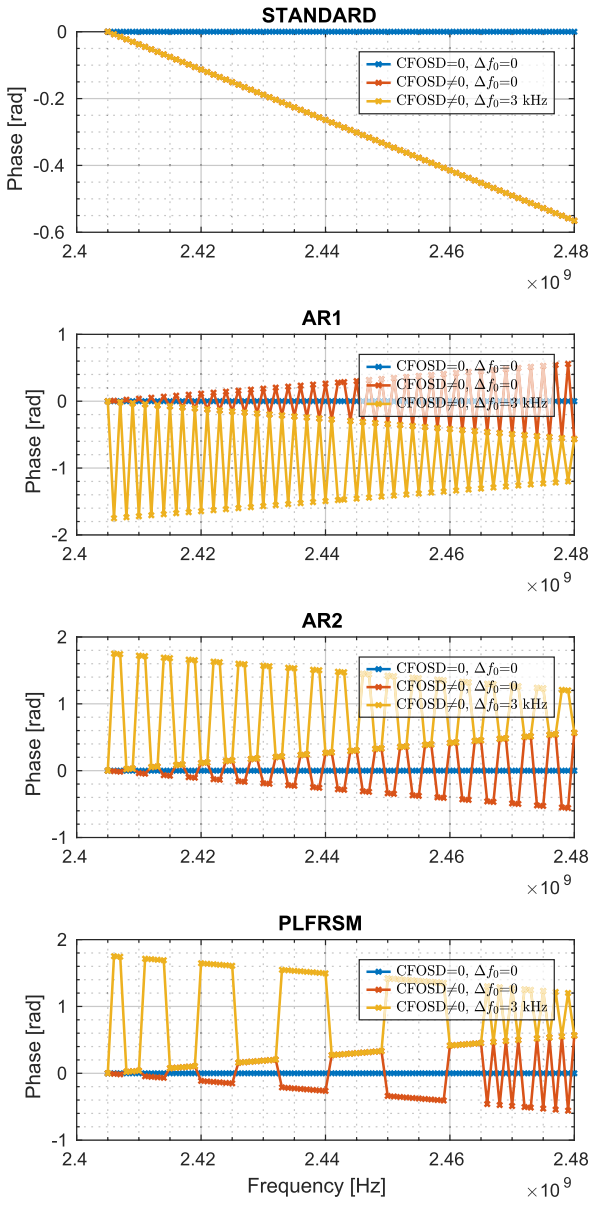

FIGURE 3. Simulated phase samples for the standard TD and the three proposed RSA-based methods. The red and yellow curves for the standard TD overlap.

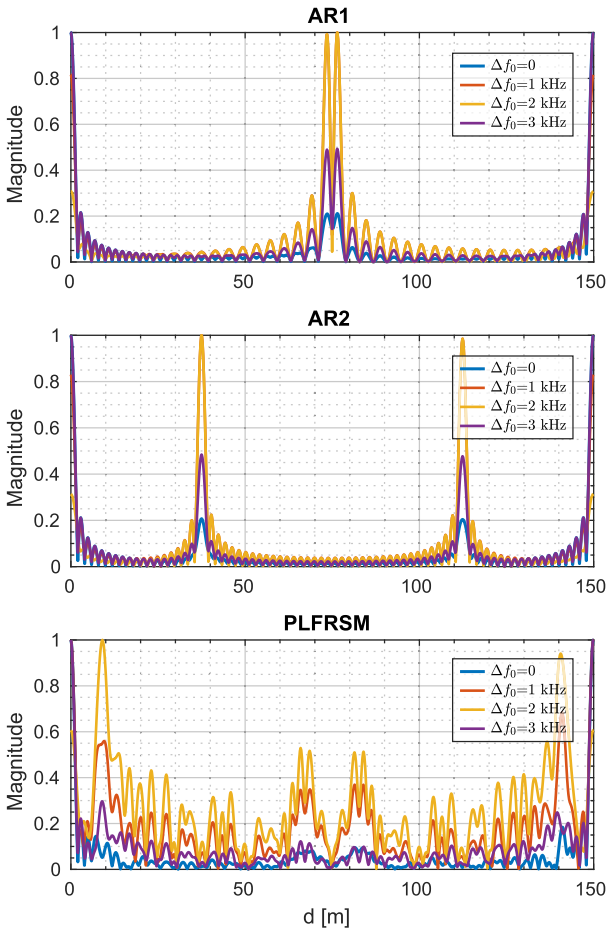

FIGURE 4. Computed CIR magnitudes for the three proposed RSA-based methods for a fixed CFOSD and various values of Δf_0.

The AR1 method for $\Delta f_0 = 0$ and CFOSD $\neq 0$ (red curve) produces phase samples for carriers with standard roles that follow the same phase trend as in the standard TD approach, while samples for carriers with reversed roles follow the same trend but with the opposite sign. As a result, the overall phase slope across carriers is close to zero. A consequence of the alternating roles is the presence of phase jumps at each role switch, as the second phase term in (13) changes sign. For $\Delta f_0 \neq 0$, the phase jumps at each role switch become more pronounced, since the first phase term in (13) also changes sign when the roles are reversed, as shown by the yellow curve. This increases the magnitude of each phase jump by twice the contribution of this phase term, which is independent of i and therefore the same for all carriers when a role switch occurs. The parameters ΔT_o and f_{IF} can be chosen so that their contribution to the overall phase jump is an integer multiple of 2π, ensuring that they do not introduce an additional phase jump, as done in the simulations. In contrast, Δf_0 is not known in advance.

The corresponding CIRs in Fig. 4 show that Δf_0 can have a strong impact on the estimated CIR. Due to the way AR1 defines the *RP*, which determines the carrier indices with role switches and associated phase jumps, the AR1 method generates two closely spaced artificial peaks that appear approximately halfway across the distance domain relative to the LOS peak. The magnitudes of these artificial peaks, as well as the magnitude of the LOS peak, depend on Δf_0. For certain values of Δf_0, the LOS peak becomes smaller than the artificial peaks, which requires a more advanced algorithm for reliable LOS detection and distance estimation.

Similar observations can be made for the AR2 and PLFRSM methods, with phase jumps occurring at positions determined by their respective *RP* patterns. For AR2, the computed CIRs also contain two artificial peaks, but due to the lower role-switching rate, they are located farther apart than in AR1. In the case of PLFRSM, the artificial path components are spread across the entire distance domain.

With a design similar to PLFRSM, the artifacts introduced by the phase jumps can be shaped so that the resulting CIR more closely resembles a noise-like spectrum rather than having a small number of dominant peaks.

To understand the effect of a particular *RP* on the estimated CIR, we examine the complex samples derived from (6). We approximate $2 + k_{\mathrm{CFO},I} + k_{\mathrm{CFO},R} \approx 2$ and omit the phase shift of the third phase term, which does not depend on the carrier index and contributes only to a global phase rotation, and therefore does not influence the CIR magnitude. The complex sample for the i-th carrier can then be written as

$$\begin{aligned} c^{(i)} = A \cdot \exp\big(j\,2\pi\,(f_{IF} + \Delta f_0)\,\Delta T_o \cdot RP[i]\big) \\ \cdot \exp\big(j\,2\pi\,(k_{\mathrm{CFO},I} - k_{\mathrm{CFO},R})\,i\,\nu\,\Delta T_o \cdot RP[i]\big) \\ \cdot \exp\big(-j\,4\pi\,i\,\nu\,d/c\big), \end{aligned} \tag{16}$$

where A is the received signal amplitude. For clarity, we define the three phase components as

$$\begin{aligned} \phi_{\Delta f_0} &= 2\pi\,(f_{IF} + \Delta f_0)\,\Delta T_o \cdot RP[i], \\ \phi_{\mathrm{CFOSD}}[i] &= 2\pi\,(k_{\mathrm{CFO},I} - k_{\mathrm{CFO},R})\,i\,\nu\,\Delta T_o \cdot RP[i], \\ \phi_d[i] &= -4\pi\,i\,\nu\,\frac{d}{c}. \end{aligned} \tag{17}$$

The CIR can be obtained using the Fourier transform property that multiplication in the frequency domain corresponds to circular convolution in the time domain ($\mathcal{F}\{s[t] \circledast h[t]\} = S[i] \cdot H[i]$):

$$\begin{aligned} h[t] = \mathrm{IFFT}\big\{A \cdot \exp\big(j \cdot \phi_d[i]\big)\big\} \\ \circledast \mathrm{IFFT}\big\{\exp\big(j \cdot \phi_{\mathrm{CFOSD}}[i]\big)\big\} \\ \circledast \mathrm{IFFT}\big\{\exp\big(j \cdot \phi_{\Delta f_0}[i]\big)\big\}. \end{aligned} \tag{18}$$

Equation (18) shows that the ideal CIR, represented by $\mathrm{IFFT}\{A \cdot \exp\big(j \cdot \phi_d[i]\big)\}$, is circularly convolved with two additional impulse responses: $\mathrm{IFFT}\{\exp\big(j \cdot \phi_{\mathrm{CFOSD}}[i]\big)\}$ and $\mathrm{IFFT}\{\exp\big(j \cdot \phi_{\Delta f_0}\big)\}$. The first impulse response depends on CFOSD and *RP*, while the second depends on Δf_0 and *RP*. An appropriate choice of *RP* shapes these impulse responses, and their circular convolution with the ideal CIR determines the structure and amplitudes of the artificial peaks introduced by the RSA approach.

1) IMPROVED RSA

The main limitation of the RSA is that distance estimation becomes invalid when the distance is determined from the position of the largest peak in the CIR and when an artificial peak exceeds the LOS peak. This occurs for certain combinations of CFOSD and Δf_0, as shown in Fig. 5, which presents the calculated absolute error (AE) of the estimated distance over CFOSD and Δf_0 sweeps. Yellow regions indicate parameter combinations for which the estimation error is large due to incorrect peak selection.

To address this problem, we introduce improved versions of the RSA-based methods in which the TDs remain unchanged, but the peak search algorithm is enhanced by performing an additional cross-correlation of the acquired CIR with a template CIR. The distance is then estimated from the position of the dominant peak in the resulting cross-correlation function. For each RSA method, a CIR template is generated by simulation for $d = 0$, CFOSD $= 0$, and a suitably chosen value of Δf_0. The template value of Δf_0 is selected by searching over candidates in the range 0-4 kHz with a step of 100 Hz. For each candidate Δf_0, a template CIR is generated. This template is then cross-correlated with a set of CIRs obtained with simulation parameters $d = 0$, Δf_0 swept over the same range as the candidate Δf_0, and CFOSD swept from -10 to 10 $\frac{\mathrm{Hz}}{\mathrm{MHz}}$ with a step of 0.2 $\frac{\mathrm{Hz}}{\mathrm{MHz}}$. For each cross-correlation, the resulting AE is recorded. The optimal template value of Δf_0 is the one that minimizes the accumulated AE over all combinations of Δf_0 and CFOSD. The search range of Δf_0 is limited to 4 kHz because, for the sampling time offset difference ΔT_o considered, the phase shift term $2\pi\,\Delta f_0 \Delta T_o \cdot 2$ wraps around approximately outside this interval, and the pattern then repeats.

The improved versions of AR1, AR2, and PLFRSM are denoted as AR1-XC, AR2-XC, and PLFRSM-XC, respectively. Fig. 5 shows that the peak-search enhancement substantially reduces the occurrence of large AEs compared to basic RSA-based methods, although large AEs still occur for a limited number of parameter combinations in the AR2-XC case. Under such conditions, the maximum search range for the estimated distance can be restricted to values below the first artificial peak, or more advanced LOS detection strategies can be applied. The proposed peak-search improvement is effective because artificial peaks generated by RSA appear at predictable positions relative to the LOS peak. Even when the LOS peak is not the largest in the original CIR, cross-correlation with the template CIR exploits the entire CIR structure, including artificial peaks, and the correlation output is maximized at the delay corresponding to the LOS component.

The main drawback of the improved approach is the additional cross-correlation step, which increases computational load and memory requirements on hardware-constrained devices. However, the cross-correlation can be computed efficiently in the frequency domain as $(h \star g)[t] = \mathrm{IFFT}\{H[k]\,G^*[k]\}$, where $h[t]$ is the measured CIR, $g[t]$ is the template CIR, $H[k]$ and $G[k]$ are their discrete Fourier transforms, and $(\cdot)^*$ denotes complex conjugation. The spectrum $H[k]$ is already available from the phase measurements across carrier frequencies, and $G^*[k]$ can be precomputed and stored in memory. The incremental computational cost is therefore limited to a single element-wise complex multiplication of $H[k]$ and $G^*[k]$. Potential downsides include peak broadening and the appearance of weaker secondary artifacts introduced by the correlation operation.

C. 4-WAY RANGING WITH STANDARD AND REVERSED ROLES

The last TD design approach considered is closely related to the four-way measurement proposed in [20]. On each i-th carrier, INIT and REF first perform the standard

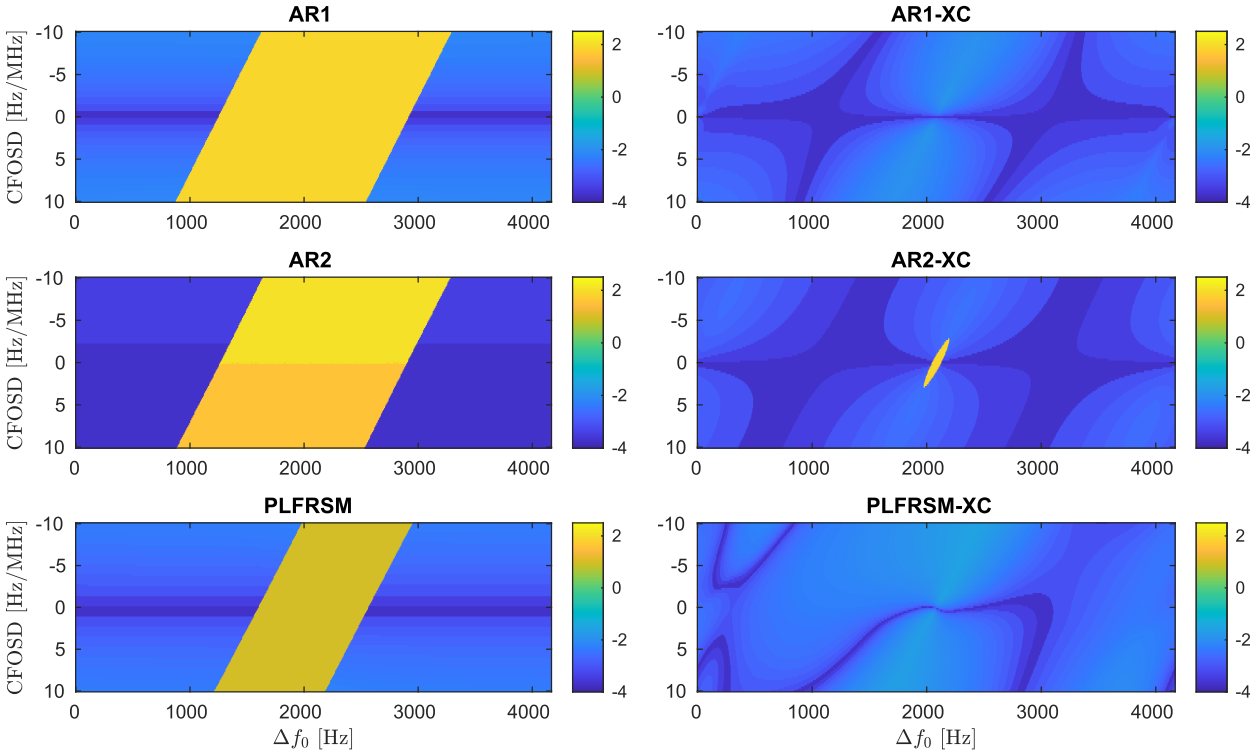

FIGURE 5. AE as a function of CFOSD and Δf_0 for the basic RSA-based methods (left) and the improved versions (right). AE is in logarithmic scale to accommodate the large variation in error magnitude.

two-way exchange, acquiring phase sample $\phi_{R,0}^{(i)}$ at REF and $\phi_{I,0}^{(i)}$ at INIT. The exchange is then repeated on the same carrier with reversed roles, acquiring $\phi_{R,1}^{(i)}$ and $\phi_{I,1}^{(i)}$ at REF and INIT, respectively. We refer to this approach as the *per-frequency role-switching approach* (PFRSA) and is illustrated in Fig. 2(e). For ease of interpretation, we assume that the second exchange starts ΔT_s after the start of the first exchange, and that the measurement on carrier $i+1$ begins $2\cdot\Delta T_s$ after the start of the measurement on carrier i. The final phase for carrier i is obtained by combining the four samples as: $\phi^{(i)} = \phi_{R,0}^{(i)} - \phi_{I,0}^{(i)} + \phi_{R,1}^{(i)} - \phi_{I,1}^{(i)}$ which evaluates to

$$\begin{aligned}\phi^{(i)} = {} & 2\pi\left(f_{IF} + \Delta f^{(i)}\right)\cdot \\ & \left[(4\cdot P[i]+1)\cdot\Delta T_s\,\frac{e_I - e_R}{1+e_I+e_R+e_I\,e_R}\right. \\ & \left. + \left(T_{o,R}+T_{o,I}\right)\frac{e_I - e_R}{1+e_I+e_R+e_I\,e_R}\right] \\ & - 4\pi\left(2f_c^{(i)} + \Delta f_I^{(i)} + \Delta f_R^{(i)} - f_{IF}\right)\frac{d}{c}. \end{aligned} \tag{19}$$

Compared to the standard TD phase in (4), the second bracketed term in PFRSA is reduced to a phase component that depends on the sum of the sampling offsets $T_{o,R}+T_{o,I}$ and is scaled by a small factor determined by the clock-drift mismatch between INIT and REF. With synchronized timing, CFOSD does not affect the measured phases and the distance estimate. The main drawback of PFRSA is its long measurement procedure, which is the longest among the approaches considered and increases the effect of timing asynchronization on distance estimation.

IV. SIMULATIONS

Numerical simulations in Matlab are used to quantify the impact of CFOSD and additive noise on MCPD distance estimation for the TD designs introduced in Section III, compared to the baseline standard TD approach. The simulation setup is defined as follows. The distance is fixed to 10 m and the received complex samples have unit magnitude on all carriers. The CIR is obtained by applying an IFFT with zero padding to 262144 points, which provides a range resolution of approximately 0.572 mm. Other simulation parameters are either specific to each simulation scenario or follow the configuration used in Sections II and III-B: $\Delta T_o = 120\ \mu$s, $\Delta T_s = 279.5\ \mu$s, $f_{IF} = 1$ MHz, $M = 76$, $f_c^{(0)} = 2405$ MHz and $\nu = 1$ MHz.

A. EFFECT OF VARYING CFOSD ON DISTANCE ESTIMATION

The first set of simulations evaluates the effect of CFOSD on the distance estimation error for the considered TD designs without additive noise. CFOSD is varied over $\pm 80\ \frac{\text{Hz}}{\text{MHz}}$ in steps of $0.02\ \frac{\text{Hz}}{\text{MHz}}$.

The simulation Scenario #1 is configured to isolate the impact of CFOSD by neglecting timing asynchronization ($e_I = e_R = 0$), setting $\Delta f_0 = 0$ kHz, and applying the sequential switching (*SS*) FSP, where carrier frequencies during the MCPD procedure are applied in ascending order

TABLE 3. CFOSD limits for RSA-based TD designs, defined as the CFOSD value beyond which the AE exceeds 0.1 m, and the corresponding mean AE within the ±CFOSD limits, for the simulation parameters of Scenario #1 ($e_I = 0$, $e_R = 0$, $\Delta f_0 = 0$ kHz, *SS* FSP) and Scenario #2 ($e_I = 10$ ppm, $e_R = 0$, $\Delta f_0 = 3$ kHz, *CycleReset(3)* FSP).

TD	Scenario #1 lower / upper limit $\left[\frac{\text{Hz}}{\text{MHz}}\right]$	Scenario #1 mean [cm]	Scenario #2 lower / upper limit $\left[\frac{\text{Hz}}{\text{MHz}}\right]$	Scenario #2 mean [cm]
AR1	-33.7 / 33.7	1.63	-1.5 / 44.4	2.14
AR2	-33.4 / 33.4	0.067	-0.4 / 51.4	0.16
PLFRSM	-34.4 / 34.4	1.04	-10.5 / 51.8	1.36
AR1-XC	-52.4 / 52.4	0.53	-49.6 / 41.4	1.89
AR2-XC	-46.0 / 46.0	0.51	-51.7 / 44.7	0.93
PLFRSM-XC	-44.6 / 39.2	0.87	-36.6 / 41.1	4.70

with $P[i] = i$ [19]. The computed AEs are shown in Fig. 6(a). The standard TD approach exhibits a linear increase in AE with increasing absolute CFOSD and has the largest errors among the considered approaches for CFOSD values away from zero. The SSTDM, DSTDM, and PFRSA TD designs maintain zero AE over the entire CFOSD sweep, confirming the wideband behavior of these designs in mitigating the effect of CFOSD on the distance estimate. The RSA-based methods exhibit nonzero AEs and a sharp increase in AE outside a certain CFOSD operating interval specific to each method. We define the CFOSD limits for RSA-based methods as the CFOSD values at which the AE exceeds 0.1 m. Table 3 summarizes the corresponding negative and positive limits, along with the mean AE within those limits. Only AR1 and PLFRSM have mean AEs above 1 cm, while the remaining RSA-based methods remain below 1 cm, with AR2 below 1 mm. Within their respective CFOSD limits, all proposed methods provide substantially improved robustness to CFOSD compared to standard TD. The cross-correlation enhanced variants extend the CFOSD operating interval in which the methods perform efficiently. The limits are symmetric for AR1, AR1-XC, AR2, and PLFRSM, while PLFRSM-XC exhibits asymmetric limits. Overall, RSA-based designs are effective and provide low bias only when the system operates within the CFOSD limits specific to each method.

The simulation Scenario #2 jointly considers CFOSD and timing asynchronization by setting $e_I = 10$ ppm and $e_R = 0$, along with a nonzero $\Delta f_0 = 3$ kHz. Carrier frequencies during the MCPD procedure are applied according to the *CycleReset(3)* FSP, which defines $P[i]$ and mitigates the impact of timing asynchronization on distance estimation [19]. The resulting AEs are shown in Fig. 6(b). In this scenario, the standard TD is biased by CFOSD. SSTDM and DSTDM again achieve the lowest AE over the entire CFOSD range, as the TD designs suppress the CFOSD contribution to overall phase while *CycleReset(3)* reduces the timing asynchronization bias. The PFRSA curve is not visible in Fig. 6(b) because its AEs exceed the plotted range. Large errors occur due to pronounced timing asynchronization effect in PFRSA, which generates large artificial peaks in the CIR specific to the *CycleReset(3)* FSP. The ability of the *CycleReset(3)* FSP to suppress timing asynchronization effects is exceeded when artificial peaks of *CycleReset(3)* induced by timing asynchronization become higher than the LOS peak, resulting in incorrect distance estimation, as observed for PFRSA. For basic RSA-based methods, the CFOSD limits are asymmetric, and the corresponding CFOSD operating interval is shifted due to the nonzero Δf_0. The lower CFOSD limits are particularly restrictive for AR1 and AR2. In contrast, AR1-XC and AR2-XC largely mitigate this effect and retain a wide CFOSD operating interval. In practice, expected CFOSD values are likely well within these limits. Although the mean AEs within the limits increase relative to Scenario #1, they remain below 1 cm for AR2 and AR2-XC. Overall, Scenario #2 highlights the coupled impact of timing asynchronization and CFOSD on distance estimation and illustrates how a more complex FSP, such as *CycleReset(3)*, interacts with the considered TD designs.

B. NOISE SENSITIVITY

The noise robustness of the proposed TD designs is evaluated using Monte Carlo simulations with additive white Gaussian noise (AWGN). Complex AWGN is added independently to each received IQ sample at INIT and REF. The CFOSD is fixed at 10 $\frac{\text{Hz}}{\text{MHz}}$, and Δf_0 is set to 3 kHz. The signal-to-noise ratio (SNR) is varied from -10 dB to 60 dB in steps of 0.1 dB. For each SNR value, 500 Monte Carlo trials are performed, and the root mean square error (RMSE) of the estimated distance is calculated. Timing asynchronization is included by setting $e_I = 10$ ppm and $e_R = 0$.

Fig. 7(a) shows the RMSE as a function of SNR for the considered TD designs when *SS* FSP is used. The *SS* FSP is biased under timing asynchronization, and since the proposed TD designs target CFOSD mitigation rather than timing asynchronization suppression, all approaches exhibit a nonzero bias at high SNR. Consequently, the RMSE curves do not converge to zero. The standard TD achieves the lowest RMSE at high SNR because, for the chosen parameters, the bias contributions from CFOSD and timing asynchronization have opposite signs and partially cancel each other. For the RSA-based methods, the RMSE at high SNR is dominated by timing asynchronization, as the CFOSD-induced bias is effectively suppressed, as shown in Section IV-A. The TDCA-based methods have the largest RMSE values, reflecting their greater sensitivity to timing asynchronization and its associated bias. As the SNR

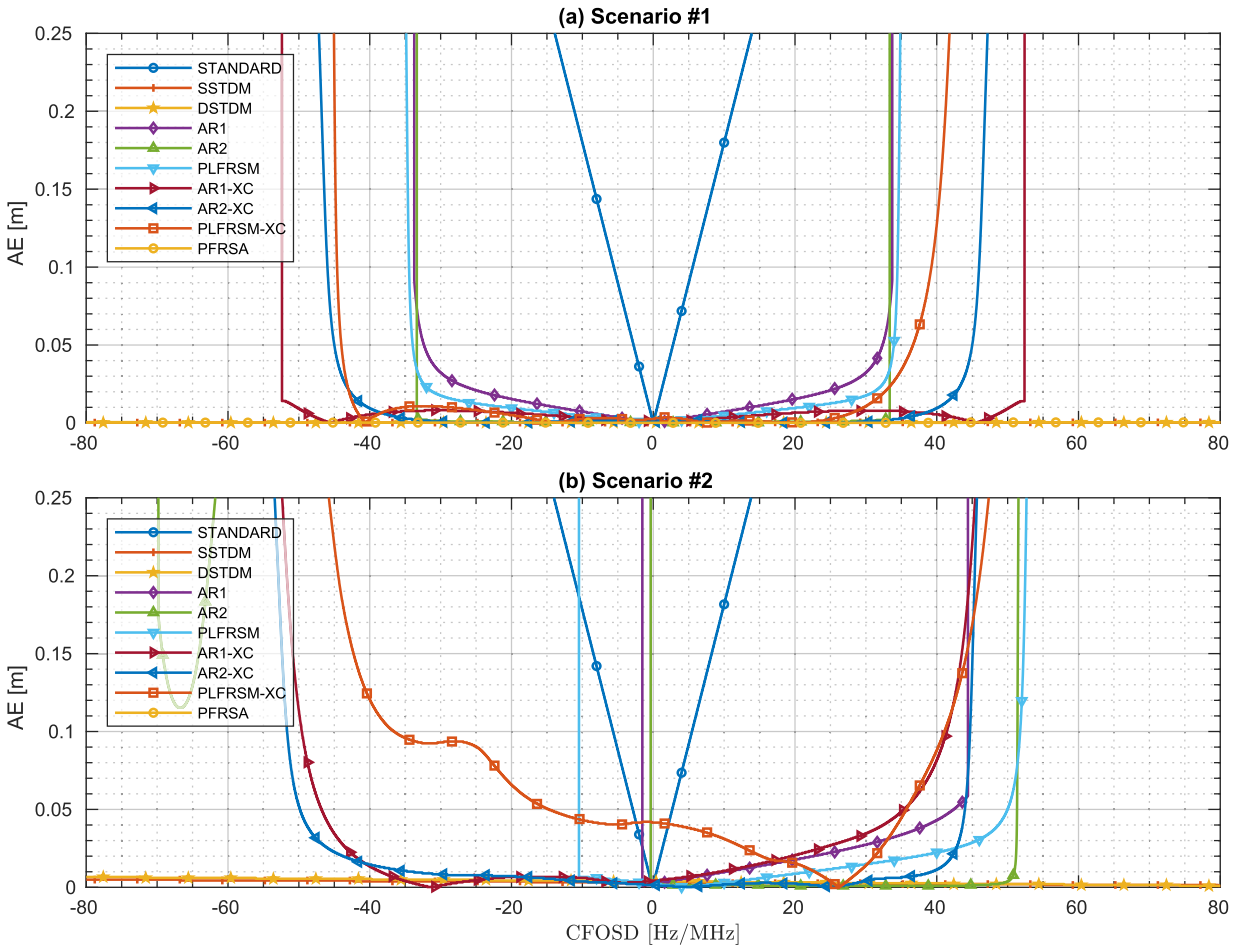

FIGURE 6. AE as a function of CFOSD for the proposed TD designs compared to the standard TD approach in two simulation scenarios: (a) Scenario #1 ($e_I = e_R = 0$, $\Delta f_0 = 0$, and *SS* FSP) and (b) Scenario #2 ($e_I = 10$ ppm, $e_R = 0$, $\Delta f_0 = 3$ kHz, and *CycleReset(3)* FSP).

decreases, all TD designs maintain an approximately constant RMSE down to a method-dependent SNR threshold, below which the RMSE increases sharply as the measurements become dominated by noise and peak selection becomes unreliable. The standard TD has the lowest threshold at approximately -1 dB. The RSA-based methods have higher thresholds, approximately between 1 dB and 4 dB. The highest threshold is observed for DSTDM at just below 7 dB, while SSTDM and PFRSA have thresholds of approximately 3 dB.

The second noise simulation scenario uses the *CycleReset(3)* FSP. The corresponding RMSE results are shown in Fig. 7(b). For all TD designs except the standard TD and PFRSA, the RMSE approaches zero at high SNR, since *CycleReset(3)* mitigates timing asynchronization and the proposed TD designs suppress the remaining CFOSD-induced bias. The standard TD has a nonzero RMSE since it does not suppress the CFOSD-induced bias. PFRSA has the largest RMSE at high SNR due to its strong sensitivity to timing asynchronization, which exceeds the mitigation capability of *CycleReset(3)* FSP and leads to the selection of an artificial peak instead of the LOS peak for distance estimation, as discussed in Section IV-A. Using *CycleReset(3)* FSP results in higher SNR thresholds for all TD designs compared to the *SS* case, consistent with the greater noise sensitivity of *CycleReset(3)* reported in [19]. Moreover, under *CycleReset(3)*, the RMSE of the RSA-based methods increases more rapidly as SNR decreases. This behavior suggests that the increased noise sensitivity is primarily introduced by the FSP selection, whereas the RSA-based TD modification alone remains comparatively less sensitive to noise, as indicated by the flatter RMSE curves obtained with *SS* FSP.

V. EXPERIMENTAL VALIDATION

Experimental validation is performed for standard TD and TD designs based on RSA to confirm the analytical and simulation results on practical hardware. RSA-based TD design methods show strong resilience to CFOSD variations and noise robustness in simulations and, among the proposed approaches, have the shortest measurement duration, making them the most suitable for practical, accurate, robust, and low-power MCPD ranging.

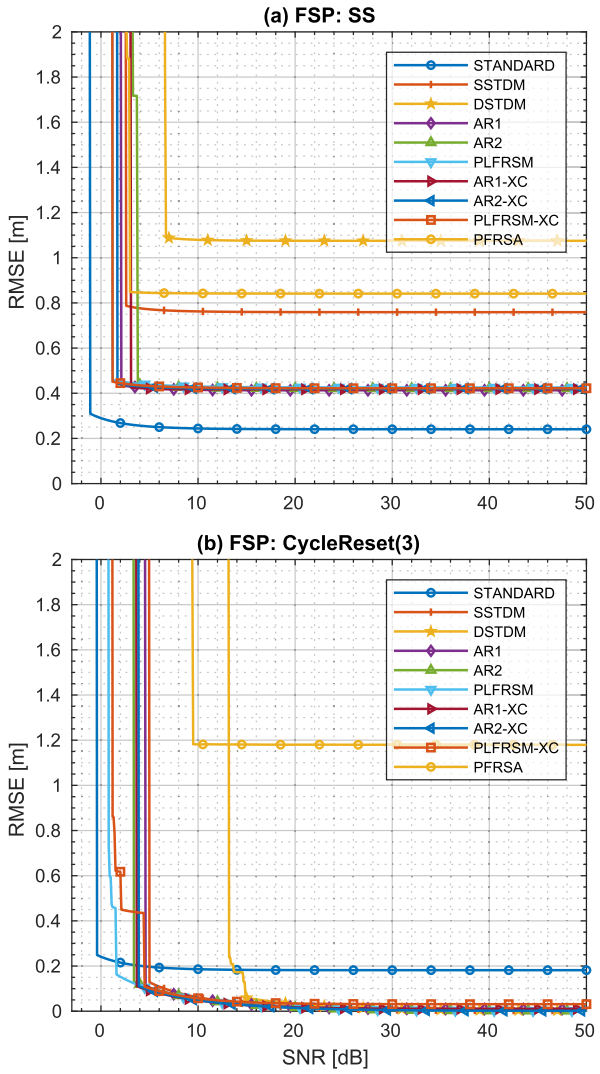

FIGURE 7. RMSE of the estimated distances as a function of SNR for the considered TD designs with fixed CFOSD, fixed Δf_0, and timing asynchronization included, using either the *SS* FSP (a) or the *CycleReset(3)* FSP (b).

The measurements are designed to assess how variations in CFOSD affect changes in the estimated distance. Absolute distance errors are not reported because the estimated propagation delay includes hardware-dependent offsets and other systematic contributions that are not directly observable. Characterizing and compensating for these offsets to achieve absolute accuracy would introduce measurement uncertainty comparable to the targeted resolution and increase sensitivity to environmental changes. Therefore, the analysis focuses on relative changes in the estimated distance as the considered parameters are varied.

Different CFOSD values are achieved by varying the CFO at REF as a function of carrier frequency in software. The smallest available CFO increment with the hardware used is 396.728 Hz, which is too coarse to generate a linear CFO ramp across the carrier frequencies corresponding to the CFOSD range of interest. Instead, a stepped approximation is

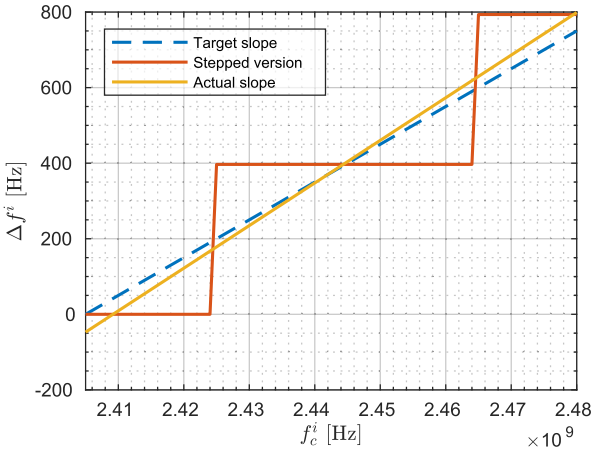

FIGURE 8. Example of CFOSD generation using stepped approximations in the experimental setup, obtained with the minimum CFO step of 396.728 Hz. The blue line shows the intended linear slope, the red line the corresponding stepped approximation, and the yellow line the actual slope estimated by simple linear regression.

used, as illustrated in Fig. 8. A set of target slopes covering the CFOSD sweep from -80 $\frac{\text{Hz}}{\text{MHz}}$ to 80 $\frac{\text{Hz}}{\text{MHz}}$ is first specified, and for each target slope, a stepped CFO profile is constructed to approximate the linear ramp using the available 396.728 Hz step. Linear regression is used to estimate the actual slope of the resulting profile. The difference between the initial CFO values at the beginning of the measured frequency band, Δf_0, is not controlled in software and remains at its default hardware-determined value unless stated otherwise. For each CFOSD configuration, 40 measurements are collected.

A. MEASUREMENT SETUP

INIT and REF are implemented using microcontroller boards equipped with AT86RF215 radio modules compliant with IEEE 802.15.4 [42]. The AT86RF215 integrates a phase measurement unit that provides access to complex IQ samples via register readout over the serial peripheral interface (SPI) bus. Measurements are conducted in a controlled manner by connecting INIT and REF with an RF coaxial cable to isolate the effect of CFOSD on distance estimation, using the same measurement setup as in [19]. Each measurement is initiated by INIT, and a wired triggering signal is provided to REF to ensure a synchronous start of the measurement procedure at both devices.

B. MEASUREMENT RESULTS

First, the CIRs obtained with the experimental setup for the RSA-based TD design methods, without cross-correlation enhancement, are compared with the simulated CIRs in Matlab to evaluate the agreement in peak shapes and locations. Simulated CIRs are generated by setting the distance d so that the LOS peaks align with the measured results and by setting $\Delta f_0 = 5.7$ kHz as an approximate value of the hardware-dependent CFO over the considered frequency band, based on previous measurements with the

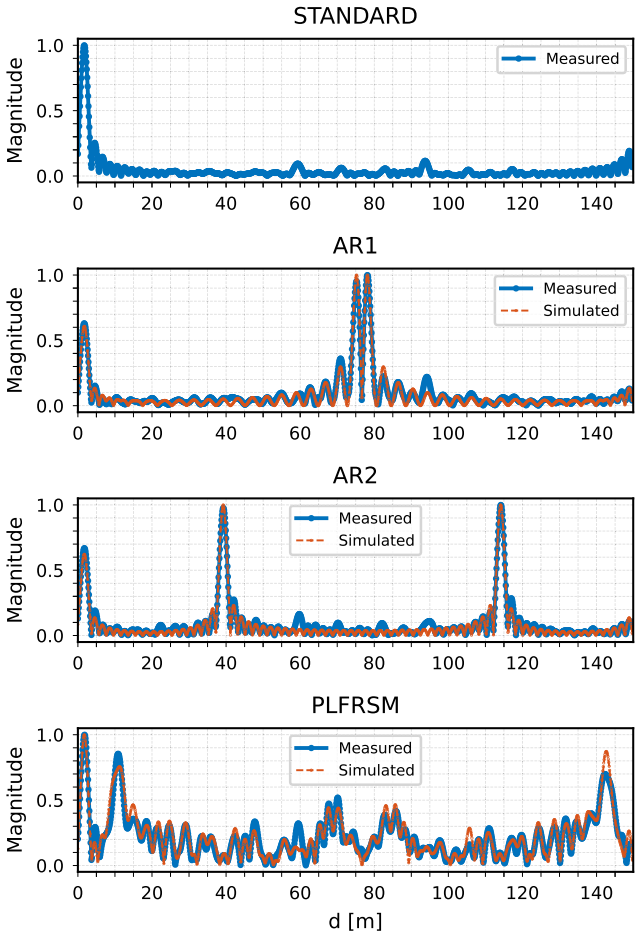

FIGURE 9. Measured and simulated CIRs for the standard TD and the three RSA-based TD designs, without cross-correlation enhancement and with CFOSD in software set to zero.

same devices. Fig. 9 presents the estimated CIRs when no CFOSD is induced in software. The CIR obtained with the standard TD is included for reference and shows a single dominant peak whose position corresponds to the measured distance. The remaining plots show the CIRs for the RSA-based methods, where the blue curves represent the measured CIRs and the red curves represent the simulated CIRs. A close agreement in peak structure and peak locations between the measured and simulated CIRs is observed for all three RSA-based methods, which supports the adopted signal model and simulation framework with the experimental observations.

To evaluate robustness to CFOSD variations, all distance estimates are reported across the induced CFOSD sweep for the standard TD and improved RSA-based methods, selected for their more robust performance. Results are shown in Fig. 10. The estimated distance for the standard TD approach shows a linear dependence on CFOSD, consistent with the distance estimate being proportional to CFOSD. In contrast, the RSA-based methods maintain an approximately constant distance estimate within their CFOSD limits, confirming a strong reduction of CFOSD-induced bias. Beyond the

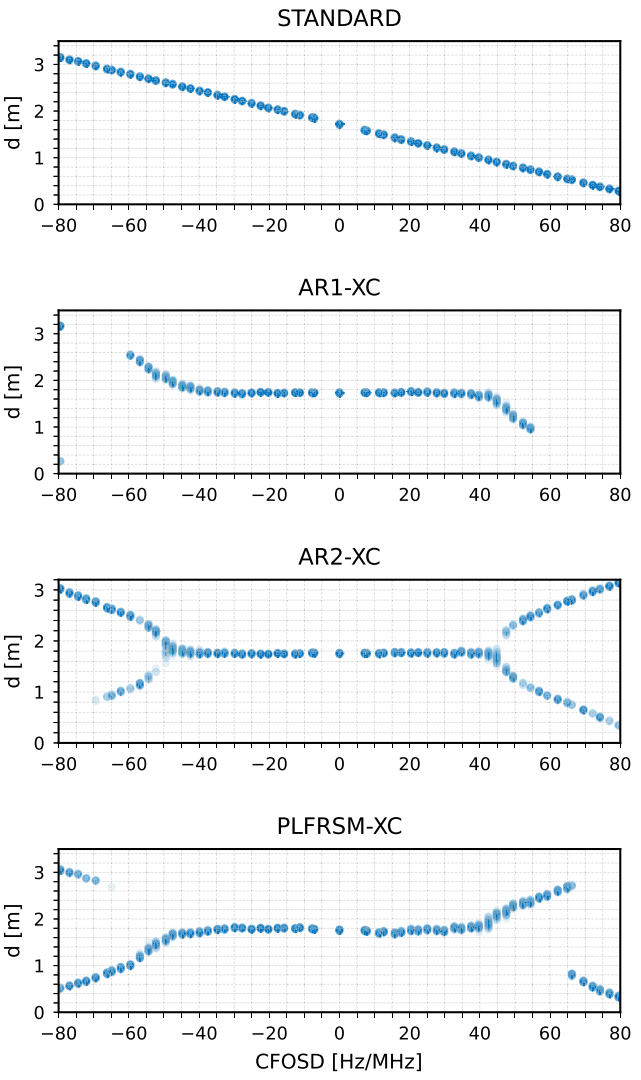

FIGURE 10. Measured distance estimates as a function of CFOSD for the standard TD and selected RSA-based TD designs, showing all 40 measurements for each CFOSD value.

TABLE 4. Slopes of the medians of estimated distances as a function of CFOSD and the standard deviations (Std dev) of the medians within the bounded CFOSD region (± 30 $\frac{\text{Hz}}{\text{MHz}}$).

TD	Slope [m·MHz / Hz]	Std dev [m]
Standard	-18.01e-3	0.3425
AR1-XC	170.68e-6	0.0094
AR2-XC	422.99e-6	0.0100
PLFRSM-XC	-1.34e-3	0.0351

CFOSD limits, the dominant LOS peak in the CIR splits into two peaks of comparable magnitude, whose separation increases with the absolute value of CFOSD, explaining the increased spread of the measured values.

The medians and standard deviations of the distance estimates computed for each CFOSD value are shown in Fig. 11. In the median plots, the red line represents a linear regression fitted to the medians within a bounded CFOSD interval of ± 30 $\frac{\text{Hz}}{\text{MHz}}$, selected to lie within the

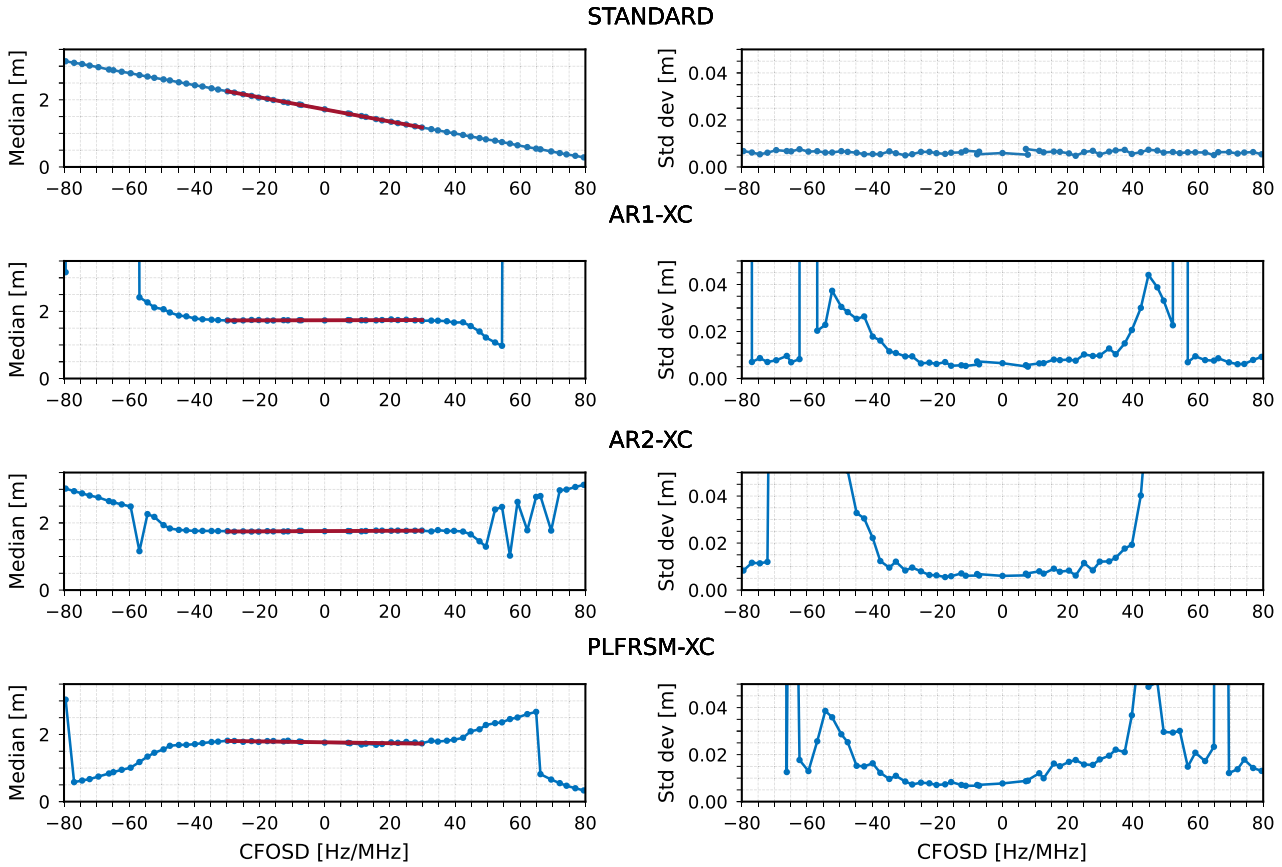

FIGURE 11. Medians (left) and standard deviations (Std dev) (right) of the estimated distance as a function of CFOSD for the standard TD and selected RSA-based TD designs, computed from 40 measurements for each CFOSD configuration. The red curve in the median plots is the fitted line obtained by simple linear regression.

TABLE 5. Qualitative comparison across TD designs. RSA-XC refers to the RSA-based method with cross-correlation-based peak selection. *In basic RSA, estimating distance from the largest peak in the CIR is sensitive to Δf_0, which can cause performance to vary under different operating conditions.

TD	CFOSD bias	Duration	Clock-drift sensitivity	Computation cost and memory footprint	Noise sensitivity	Unambiguous range
Standard	high	short	baseline	low	lowest	$c/(2\,\nu)$
SSTDM	very low	medium	high	low	medium	$c/(2\,\nu)$
DSTDM	very low	long	higher	low	medium	$c/(2\,\nu)$
RSA	variable*	short	baseline	low	low	$c/(2\,\nu)$
RSA-XC	low	short	baseline	medium	low	$c/(2\,\nu)$
PFRSA	very low	medium	highest	low	medium	$c/(4\,\nu)$

CFOSD limits of the RSA-based methods. The resulting slopes of the fitted lines, reported in Table 4, show that all RSA-based methods outperform standard TD, with AR1-XC achieving the smallest slope, followed by AR2-XC and PLFRSM-XC. A pronounced performance gap is observed between PLFRSM-XC and the other two RSA-based methods. The slope obtained for the standard TD matches the prediction of (8), which also evaluates to $-18{\cdot}10^{-3}\,\frac{\text{m·MHz}}{\text{Hz}}$ for $\Delta T_o = 120\,\mu$s. Table 4 further reports the standard deviation of the computed median distances within the bounded CFOSD interval, quantifying the spread of the median estimate under CFOSD variation. The values obtained are approximately 1 cm for AR1-XC and AR2-XC and 3.5 cm for PLFRSM-XC, which remains roughly one order of magnitude lower than for the standard TD.

The computed standard deviations for each CFOSD value show that, for small absolute values of CFOSD, the RSA-based methods have a spread of distance estimates comparable to the standard TD, indicating no increased sensitivity to measurement noise. As the CFOSD limits are approached, the standard deviation increases because the LOS peak begins to split into two peaks of similar magnitude, and for repeated measurements, the distance estimate alternates between the corresponding delays.

To evaluate the robustness of the selected TD designs to variations in Δf_0 and to quantify the benefit of cross-correlation enhancement for LOS detection in RSA-based methods, additional measurements were performed in which Δf_0 was swept from 0 to 3967 Hz in steps of 396.728 Hz alongside CFOSD. For each CFOSD and

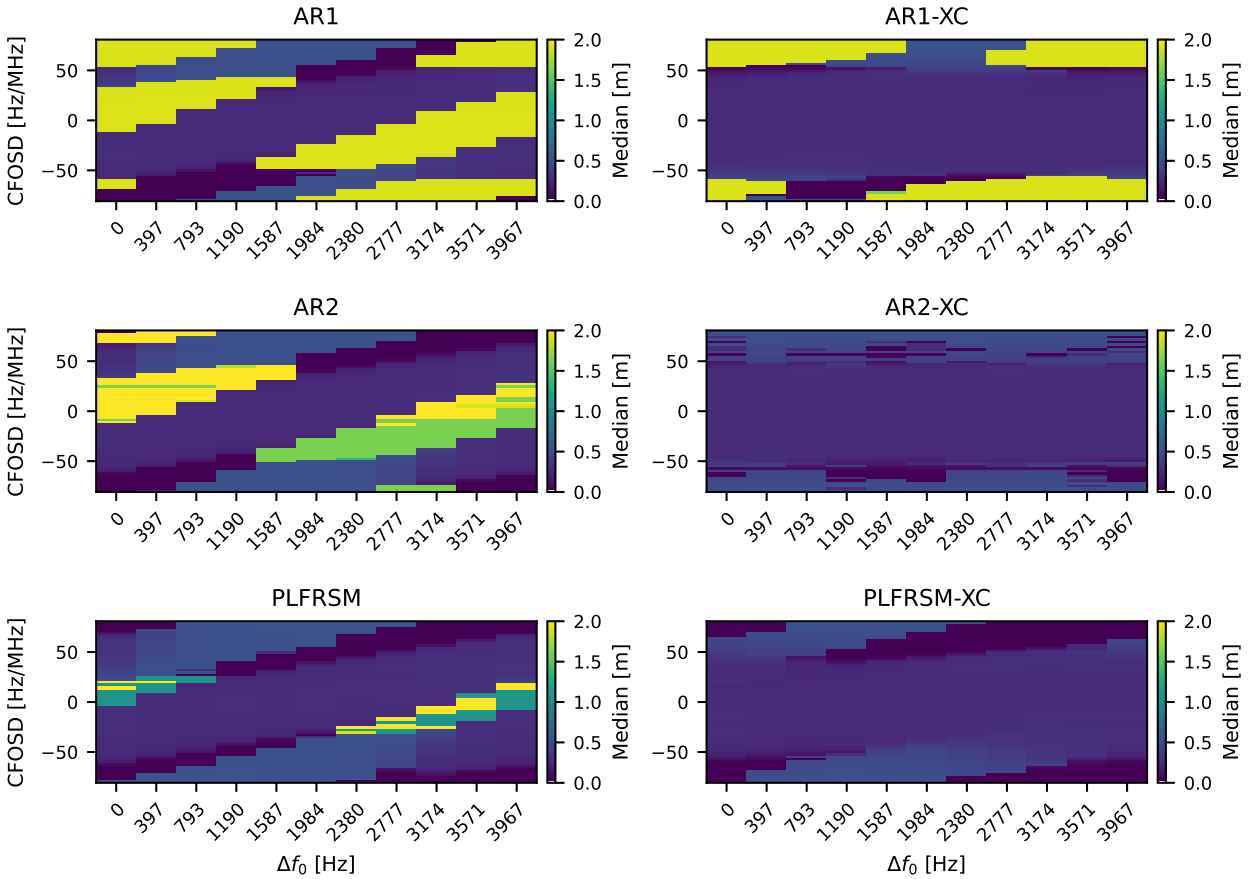

FIGURE 12. Median estimated distance as a function of CFOSD and Δf_0 for the three considered RSA-based TD designs without (left) and with (right) cross-correlation enhancement. The estimated distance is shown on a logarithmic color scale to accommodate the large variation in magnitude.

Δf_0 pair, 10 measurements were collected, and the median distance was computed, as shown in Fig. 12. The left-hand plots correspond to the basic RSA-based methods without cross-correlation enhancement. For certain combinations of CFOSD and Δf_0, large errors occur because an artificial peak is selected instead of the LOS peak, a behavior observed for all three methods. The right-hand plots show the corresponding cross-correlation enhanced variants. Within approximately $\pm 50\ \frac{\text{Hz}}{\text{MHz}}$, the uniform color indicates that the estimated distance remains constant and LOS detection is reliable. The measured results are consistent with the simulation results in Section III-B, with a horizontal shift attributed to the additional CFO contributed by the hardware, which is added to the software-controlled CFO.

VI. DISCUSSION AND CONCLUSION

This paper demonstrates that CFOSD is pronounced in devices equipped with low-cost crystal oscillators with loose tolerances and stability, and that CFOSD introduces a systematic bias in MCPD distance estimation using the standard TD. Based on a signal model for the standard TD, a closed-form expression for the distance error is derived, revealing a dominant bias term determined by CFOSD and the sampling time offset difference ΔT_o.

To mitigate CFOSD-induced bias, two TD design approaches are proposed. Simulation results with CFOSD sweep and additive noise show that TDCA-based methods suppress CFOSD-induced terms over a wide CFOSD range and achieve nearly zero bias, at the cost of longer measurement duration, increased sensitivity to timing asynchronization, and higher SNR requirements. In contrast, RSA-based methods reverse the roles of INIT and REF across carrier frequencies according to a role pattern *RP*, preserve the measurement duration of the standard TD, reduce CFOSD sensitivity within a CFOSD operating range, and require only a modest increase in SNR requirements compared to the standard TD. A cross-correlation peak-search enhancement further improves LOS selection for RSA-based methods and extends the effective CFOSD operating range.

Experimental validation is performed with standard TD and RSA-based TD design methods. Different CFOSD values are generated by applying frequency-varying CFO at REF in software. The measured CIRs closely match the simulated results in both peak structure and peak locations. Results from the CFOSD sweep confirm the linear dependence of the estimated distance on CFOSD for standard TD, while the proposed methods, particularly AR1-XC, AR2-XC, and PLFRSM-XC, maintain an approximately constant distance estimate within their optimal operating ranges.

Table 5 provides a qualitative comparison of the TD designs considered, based on analytical and simulation results. A longer measurement duration increases energy consumption and the probability of interference, reduces the refresh rate of distance updates and the data throughput available for transmission, and imposes a stricter coherence time requirement, which can limit performance under mobility or fast channel variation.

Although the signal model and validation consider a single-path channel, the expected behavior in a multipath channel follows directly from the given signal model. The asynchronization-induced phase term is common to all path components at a given carrier because it is generated by the transceiver oscillators rather than by propagation. Consequently, (16) can be extended to a multipath channel scenario by replacing the single exponential describing the propagation phase shift with a sum of complex path contributions over all path components at that carrier, while the asynchronization-induced terms remain unchanged. From the CFR-to-CIR relationship (18), it follows that the asynchronization-induced artificial peaks in the CIR are present for each path component. A detailed analysis is left for future work.

The choice of an optimal *RP* for RSA depends on the application. The *RP*s proposed in this paper primarily illustrate how different designs affect the CIR and how distance estimation is influenced by CFOSD. Future work will investigate *RP* designs that are more robust to CFOSD and Δf_0 variations, and will study the joint optimization of *RP* and FSP to improve robustness to both CFOSD and timing asynchronization.

REFERENCES

[1] K. Wu, J. Pegoraro, F. Meneghello, J. A. Zhang, J. O. Lacruz, J. Widmer, F. Restuccia, M. Rossi, X. Huang, D. Zhang, G. Caire, and Y. J. Guo, "Sensing in bistatic ISAC systems with clock asynchronism: A signal processing perspective," *IEEE Signal Process. Mag.*, vol. 41, no. 5, pp. 31–43, Sep. 2024.

[2] H. Ólafsdóttir, A. Ranganathan, and S. Capkun, "On the security of carrier phase-based ranging," in *Cryptographic Hardware and Embedded Systems—CHES 2017*, vol. 10529, W. Fischer and N. Homma, Eds., Cham, Switzerland: Springer, Aug. 2017, pp. 490–509.

[3] J. A. Zhang, K. Wu, X. Huang, Y. J. Guo, D. Zhang, and R. W. Heath Jr., "Integration of radar sensing into communications with asynchronous transceivers," *IEEE Commun. Mag.*, vol. 60, no. 11, pp. 106–112, Nov. 2022.

[4] Z. Bin Tariq, J. P. Van Marter, A. G. Dabak, N. Al-Dhahir, and M. Torlak, "Reduced complexity deep learning approach for Bluetooth ranging in multipath environments," *IEEE Sensors J.*, vol. 24, no. 19, pp. 31431–31441, Oct. 2024.

[5] W. Kluge and E. Sachse, "Circuit and method for distance measurement between two nodes of a radio network," U.S. Patent 20 110 006 942 A1, Jan. 2011. [Online]. Available: https://patents.google.com/patent/US20110006942A1/en

[6] K. Balakrishnan, R. Dhanalakshmi, B. B. Sinha, and R. Gopalakrishnan, "Clock synchronization in industrial Internet of Things and potential works in precision time protocol: Review, challenges and future directions," *Int. J. Cognit. Comput. Eng.*, vol. 4, pp. 205–219, Jun. 2023.

[7] A. A. Nasir, S. Durrani, H. Mehrpouyan, S. D. Blostein, and R. A. Kennedy, "Timing and carrier synchronization in wireless communication systems: A survey and classification of research in the last 5 years," *EURASIP J. Wireless Commun. Netw.*, vol. 2016, no. 1, p. 180, Dec. 2016.

[8] M. Pelka, D. Amann, M. Cimdins, and H. Hellbriick, "Evaluation of time-based ranging methods: Does the choice matter?" in *Proc. 14th Workshop Positioning, Navigat. Commun. (WPNC)*, Oct. 2017, pp. 1–6.

[9] I. Kravets, N. Kotliar, O. Karpin, and A. Luchechko, "BLE phase-based ranging: Accuracy and capability under strong Wi-Fi interference," *Int. J. Electron. Telecommun.*, vol. 71, no. 3, pp. 1–7, 2025, doi: 10.24425/ijet.2025.153626.

[10] A. Santra, I. Kravets, N. Kotliar, and A. Pandey, "Enhancing Bluetooth channel sounding performance in complex indoor environments," *IEEE Sensors Lett.*, vol. 8, no. 10, pp. 1–4, Oct. 2024.

[11] Y. Schröder and L. Wolf, "InPhase: Phase-based ranging and localization," *ACM Trans. Sensor Netw.*, vol. 18, no. 2, pp. 1–39, Jan. 2022.

[12] M. Nikodem, G. Trajnowicz, G. S. de Blasio, and F. A. Quesada-Arencibia, "Experimental evaluation of multicarrier phase difference localization in Bluetooth low energy," *IEEE Sensors J.*, vol. 25, no. 1, pp. 1548–1560, Jan. 2025.

[13] S. Cortesi, C. Vogt, and M. Magno, "Comparison between an RSSI- and an MCPD-based BLE indoor localization system," *Computers*, vol. 12, no. 3, p. 59, Mar. 2023.

[14] M. Gunia, A. Zinke, N. Joram, and F. Ellinger, "Setting up a phase-based positioning system using off-the-shelf components," in *Proc. 14th Workshop Positioning, Navigat. Commun. (WPNC)*, Oct. 2017, pp. 1–6.

[15] P. Zand, J. Romme, J. Govers, F. Pasveer, and G. Dolmans, "A high-accuracy phase-based ranging solution with Bluetooth low energy (BLE)," in *Proc. IEEE Wireless Commun. Netw. Conf. (WCNC)*, Apr. 2019, pp. 1–8.

[16] P. Zand, A. Duzen, J. Romme, J. Govers, C. Bachmann, and K. Philips, "A high-accuracy concurrent phase-based ranging for large-scale dense BLE network," in *Proc. IEEE 30th Annu. Int. Symp. Pers., Indoor Mobile Radio Commun. (PIMRC)*, Sep. 2019, pp. 1–7.

[17] A. Duzen, "Implementation and evaluation of phase-based group ranging and localization with BLE," M.S. thesis, Dept. Elect. Eng., Electron. Syst. Res. Group, Eindhoven Univ. Technol., Eindhoven, The Netherlands, Aug. 2019.

[18] M. Pelka, C. Bollmeyer, and H. Hellbruck, "Accurate radio distance estimation by phase measurements with multiple frequencies," in *Proc. Int. Conf. Indoor Positioning Indoor Navigat. (IPIN)*, Oct. 2014, pp. 142–151.

[19] A. Simončič, G. Morano, A. Hrovat, and T. Javornik, "Optimizing frequency switching pattern to reduce asynchronization effect in MCPD ranging systems," *IEEE Access*, vol. 13, pp. 169791–169811, 2025.

[20] M. Oshiro, S. Otaka, T. Kato, K. Nonin, M. Nishikawa, Y. Nito, H. Ishiwata, and H. Yoshida, "Sub-GHz phase-based ranging system: Implementation and evaluation," in *Proc. IEEE 91st Veh. Technol. Conf. (VTC-Spring)*, Belgium, May 2020, pp. 1–7.

[21] *IEEE Standard for Low-Rate Wireless Networks—Amendment 1: Enhanced Ultra Wideband (UWB) Physical Layers (PHYs) and Associated Ranging Techniques*, IEEE Standard Std 802.15.4z-2020, Aug. 2020, pp. 1–174.

[22] J. Ma, F. Zhang, B. Jin, C. Su, S. Li, Z. Wang, and J. Ni, "Push the limit of highly accurate ranging on commercial UWB devices," *Proc. ACM Interact., Mobile, Wearable Ubiquitous Technol.*, vol. 8, no. 2, pp. 1–27, May 2024.

[23] D. Neirynck, E. Luk, and M. McLaughlin, "An alternative double-sided two-way ranging method," in *Proc. 13th Workshop Positioning, Navigat. Commun. (WPNC)*, Oct. 2016, pp. 1–4.

[24] M. Kwak and J. Chong, "A new double two-way ranging algorithm for ranging system," in *Proc. 2nd IEEE InternationalConference Netw. Infrastructure Digit. Content*, Sep. 2010, pp. 470–473.

[25] Y. Jiang and V. C. M. Leung, "An asymmetric double sided two-way ranging for crystal offset," in *Proc. Int. Symp. Signals, Syst. Electron.*, Jul. 2007, pp. 525–528.

[26] J. X. Lee, Z. Lin, and F. C. P. Shin, "Symmetric double side two way ranging with unequal reply time," in *Proc. IEEE 66th Veh. Technol. Conf.*, Sep. 2007, pp. 1980–1983.

[27] M. A. Shalaby, C. C. Cossette, J. R. Forbes, and J. Le Ny, "Reducing two-way ranging variance by signal-timing optimization," *IEEE Trans. Aerosp. Electron. Syst.*, vol. 60, no. 3, pp. 3718–3724, Jun. 2024.

[28] M. Pelka and H. Hellbruck, "S-TDoA-sequential time difference of arrival—A scalable and synchronization free approach forl positioning," in *Proc. IEEE Wireless Commun. Netw. Conf.*, Apr. 2016, pp. 1–6.

[29] Y. Lin, T. Guo, M. Guo, and Y. Fu, "Motion compensation for SAA FMCW radar based on specific switching scheme," *Appl. Sci.*, vol. 9, no. 17, p. 3441, Aug. 2019.

[30] Y. Lin, K. Yang, M. Guo, and Y. Fu, "Elimination of motion-induced phase based on double-time switching scheme for SAA FMCW radar," *Electronics*, vol. 8, no. 7, p. 786, Jul. 2019.
[31] P. Feil, "Optimizing switching sequence in the case of switched antenna arrays," U.S. Patent 20 120 182 174 A1, Jul. 2012. Accessed: Feb. 16, 2026. [Online]. Available: https://patents.google.com/patent/US20120182174A1/en
[32] C. Hu, Y. Liu, H. Meng, and X. Wang, "Randomized switched antenna array FMCW radar for automotive applications," *IEEE Trans. Veh. Technol.*, vol. 63, no. 8, pp. 3624–3641, Oct. 2014.
[33] A. Al-Ameri, J. Park, J. Sanchez, X. Cai, and F. Tufvesson, "A hybrid antenna switching scheme for dynamic channel sounding," in *Proc. IEEE 97th Veh. Technol. Conf. (VTC-Spring)*, Jun. 2023, pp. 1–6.
[34] R. Wang, O. Renaudin, C. U. Bas, S. Sangodoyin, and A. F. Molisch, "On channel sounding with switched arrays in fast time-varying channels," *IEEE Trans. Wireless Commun.*, vol. 18, no. 8, pp. 3843–3855, Aug. 2019.
[35] T. Pedersen, C. Pedersen, X. Yin, B. H. Fleury, R. R. Pedersen, B. Bozinovska, A. Hviid, P. Jourdan, and A. Stucki, "Joint estimation of Doppler frequency and directions in channel sounding using switched Tx and Rx arrays," in *Proc. IEEE Global Telecommun. Conf.*, vol. 4, Nov. 2004, pp. 2354–2360.
[36] T. Pedersen, C. Pedersen, X. Yin, and B. H. Fleury, "Optimization of spatiotemporal apertures in channel sounding," *IEEE Trans. Signal Process.*, vol. 56, no. 10, pp. 4810–4824, Oct. 2008.
[37] J. Sanchez, X. Cai, A. Al-Ameri, and F. Tufvesson, "Low-complexity optimization of antenna switching schemes for dynamic channel sounding," *IEEE Trans. Wireless Commun.*, vol. 25, pp. 7729–7743, 2026.
[38] A. Simončič, K. Guan, G. Morano, A. Švigelj, A. Hrovat, T. Kocevska, and T. Javornik, "Experimental evaluation of enhanced antenna switching for CFO mitigation in DoA estimation," *IEEE Open J. Antennas Propag.*, vol. 6, pp. 1022–1036, 2025.
[39] P. Avital, G. Chardon, and J. Picheral, "Design of switching sequences for sine parameters estimation on switched antenna arrays," *Signal Process.*, vol. 188, Nov. 2021, Art. no. 108244.
[40] Atmel Corporation. (2016). *AT86RF215 Datasheet*. Accessed: Oct. 15, 2025. [Online]. Available: https://www.microchip.com/en-us/product/at86rf215
[41] Y. Xie, Z. Li, and M. Li, "Precise power delay profiling with commodity Wi-Fi," *IEEE Trans. Mobile Comput.*, vol. 18, no. 6, pp. 1342–1355, Jun. 2019.
[42] G. Morano, A. Simončič, T. Kocevska, T. Javornik, and A. Hrovat, "Distance- and angle-based hybrid localization integrated in the IEEE 802.15.4 TSCH communication protocol," *Sensors*, vol. 24, no. 12, p. 3925, Jun. 2024.

ALEŠ SIMONČIČ (Student Member, IEEE) received the B.Sc. and M.Sc. degrees in electrical engineering from the University of Ljubljana, in 2019 and 2022, respectively. He is currently pursuing the Ph.D. degree in information and communication technologies with the Jožef Stefan International Postgraduate School.

He is currently a Young Researcher with the Department of Communication Systems, Jožef Stefan Institute, Ljubljana. His master's thesis focused on the estimation of the angle of arrival using BLE technology and antenna arrays. His research interests include radio communication systems, particularly protocols, antennas and arrays, direction of arrival estimation methods, embedded systems, and radio environment characterization.

GREGA MORANO (Graduate Student Member, IEEE) received the M.Sc. degree in electrical engineering from the University of Ljubljana, in 2021. He is currently pursuing the Ph.D. degree in information and communication technologies with the Jožef Stefan International Postgraduate School.

He is currently a Research Assistant with the Department of Communication Systems, Jožef Stefan Institute, Ljubljana. His research interests include the IoT communication protocols, wireless localization, integrated sensing and communication, embedded systems, wireless sensor networks, and wireless experimental testbeds.

ANDREJ HROVAT (Member, IEEE) received the B.Sc. and M.Sc. degrees in electrical engineering from the University of Ljubljana, in 2004 and 2008, and the Ph.D. degree from the Jožef Stefan International Postgraduate School, in 2011.

Since 2004, he has been with the Department of Communication Systems, Jožef Stefan Institute. He is currently holding the position of a Senior Research Fellow. He works on several projects connected with professional mobile communication systems, 2G-5G, WiFi and the IoT technologies, satellite and sensor networks, including several COST actions, Framework Program projects, H2020 Projects, European Space Agency (ESA) Projects, and numerous national research and application projects. He is the author or co-author of more than 120 peer-reviewed journal and conference papers. His research and working experience are in telecommunications, focusing on development and performance analysis for fixed and mobile systems, including terrestrial, stratospheric, and satellite systems, and radio-channel modeling for fixed and mobile narrowband and broadband radio communication systems. He is a TCP member for various international conferences and workshops. He serves as a journal editorial board member and the guest editor. He is a reviewer for several international impact-factor journals.

TOMAŽ JAVORNIK (Member, IEEE) received the B.Sc., M.Sc., and Ph.D. degrees in electrical engineering from the University of Ljubljana, Ljubljana, Slovenia, in 1987, 1990, and 1993, respectively.

He is currently a Scientific Counsellor with the Communication Systems Department, Jožef Stefan Institute, Ljubljana, and an Assistant Professor with the Jožef Stefan International Postgraduate School, Ljubljana. He participated in several COST and Framework Programme Projects. He has co-authored more than 100 refereed journal and conference papers and several books and book chapters in mobile and wireless communications. He holds two international patents. His research experience interests include telecommunications, focusing on the development and performance analysis of fixed and mobile systems, radio-channel measurements, modeling and simulations, and indoor localization. He serves as a TPC member or a reviewer for several IEEE conferences and journals.